Journal of Computational Physics 505 (2024) 112907

Contents lists available at ScienceDirect

Journal of Computational Physics

journal homepage: www.elsevier.com/locate/jcp

Multi-component electro-hydro-thermodynamic model with phase-field method. I. Dielectric

Haodong Zhang [a,b], Fei Wang [a,b,*], Britta Nestler [a,c]

[a] Institute of Applied Materials-Microstructure Modelling and Simulation, Karlsruhe Institute of Technology (KIT), Strasse am Forum 7, Karlsruhe, 76131, Germany

[b] Institute of Nanotechnology, Karlsruhe Institute of Technology (KIT), Hermann-von-Helmholtz-Platz 1, Eggenstein-Leopoldshafen, 76344, Germany

[c] Institute of Digital Materials Science, Karlsruhe University of Applied Sciences, Moltkestrasse 30, Karlsruhe, 76133, Germany

ARTICLE INFO

Keywords:
Electro-hydro-thermodynamic model
Phase-field method
Multicomponent
Phase separation
Phase diagram

ABSTRACT

We derive a multi-component electro-hydro-thermodynamic (EHTD) model for both leaky and perfect dielectric materials via the principle of energy dissipation. Differing from previous electro-hydrodynamic (EHD) models focusing on fluid mechanics, the electrochemical potential expression is revised and the electric field related term is added to the mass and momentum conservation equations. Resulting from this new correction, we obtain a generalized electro-hydro-thermodynamic stress tensor including the effect of Kortweg and Maxwell stresses. We observe the magnificent impact of the electric field on the thermodynamic equilibrium of the system in two aspects: (i) phase diagram modified by the electric field; (ii) electric field induced surface tension decrease/increase. In addition, the proposed model is validated and shows well conformity with previous analytical solutions in literature. As exemplary applications, we perform phase-field simulations to study the ternary droplet coalescence and spinodal decomposition and observe several typical morphological transformations, such as satellite drop formation and Quincke rotation.

1. Introduction

The electrohydrodynamics (EHD) of fluid has been studied for decades and bred great amounts of contemplation to understand the fluid behavior affected by the electric field. The most fundamental study on dielectric materials is established on the pioneer and fundamental study of Taylor [1] and Melcher [2]. In this theoretical model, the droplet is slightly deformed by the uniform electric field and its equilibrium shape is highly correlated with its electrical properties, such as the permittivity ε and conductivity σ. Later, Feng [3] improved Taylor's theory and derived the droplet deformation in the 2-dimensional case, which matches well with experiments. However, these predictions are strongly restricted by the limit of small deformation which is inapplicable to many industrial processes, such as the electrospinning & electrospraying process and electric field enhanced droplet coalescence. Numerical simulation can overcome these limitations by modeling the interplay of fluid flow, droplet deformation, and interfacial charges in a set of mathematical physical equations.

The milestones of the mathematical approach to EHD are well documented in the quintessential work of Stratton [4] and Saville [5], where the coupling of Navier-Stokes equations with Gauss's law is derived. To solve the complex electro-hydrodynamics

* Corresponding author.
E-mail address: fei.wang@kit.edu (F. Wang).

https://doi.org/10.1016/j.jcp.2024.112907
Received 14 July 2023; Received in revised form 29 February 2024; Accepted 1 March 2024

Available online 7 March 2024

of fluids, two popular models, namely, the sharp interface and the diffuse interface models, are profoundly applied. Belonging to the former group, the level-set method (LS) has been widely adopted for years to simulate the electric field enhanced droplet deformation [6], liquid fuel injection [7]. Another important approach is the volume-of-fluid (VOF) which assists in the investigation of droplet coalescence [8], bubble deformation [9], and droplet emulsification [10] inside the electric field. Other sharp interface models, such as the boundary integral method [11,12], front-tracking method [13], have also achieved a great number of accomplishments in the droplet-matrix binary system. The great advantages of these sharp interface models are their high efficiency, robustness, and ease of implementation. However, these models suffer from mass conservation and implementation of surface tension force. For instance, the LS method has a mass conservation problem. Some intermediate algorithm steps are needed to smoothen the composition profile across the interface to preserve the mass [14]. For the VOF method, there is an unsettled knotty issue: the treatment of the interface and the resulting surface tension force. The most common approach is to assign a finite interface, rather than zero thickness. With a selected distribution function, the property changes across the interface are estimated. The calculation of the surface tension force crucially relies on a smooth function that numerically allocates the force onto the finite thickness. This approach can lead to nonphysical interfacial spurious currents, which are eliminated by numerical algorithms to reconstruct the curvature and normal directions at the interface location [15].

In contrast to this, the diffuse interface methods show the power by modeling the interface as a diffused thick layer [16–18]. For instance, the phase-field method gains its popularity through the ingenious yet simple implementation of different fields for complex physical scenarios [19]. First proposed by Lin and Carlson [20], the EHD phase-field model with Cahn-Hilliard-Navier-Stokes equations has been applied to simulate many electrohydrodynamic related processes, such as eletroprinting [21] and electropatterning [22,23]. In the Cahn-Hilliard (CH) approach, the droplet-matrix interface varies continuously from the equilibrium droplet composition to the equilibrium matrix composition. Especially, the composition profile c across the interface is iterated towards the equilibrium which is defined by the uniform chemical potential μ and homogeneous Landau potential (also known as grand potential) inside the whole domain. Meanwhile, the surface tension force is more easily interpreted as $-c\nabla\mu$ [24,25] which eases the burden of calculating the curvature and normal direction. Besides, the Allen-Cahn type (AC) phase-field model is also reported in [26]. Compared with the CH model, this approach has a higher numerical efficiency but possesses an apparent drawback with respect to volume conservation. To preserve the volume, Ref. [26] neglected the curvature effect by canceling the curvature-related term in the chemical potential μ. Obviously, this treatment is only valid for the single droplet setup where the fluid flow overwhelms the diffusion. For the droplet coalescence and liquid phase separation where interface curvature changes drastically with time, this AC model is incapable of resolving the correct dynamics.

In some literature, the surface tension force takes the formulation of $\mu\nabla c$ which is the Legendre transformation of $-c\nabla\mu$. Both formulations are correct if the chemical free energy density f is symmetric to the composition c and the equilibrium chemical potential is 0 according to the far field condition. But for the system with an asymmetric f, such as the polymeric fluid described by the Flory-Huggins theory [27,28], $-c\nabla\mu$ is the only adoption. In addition, the electric field can change the free energy into asymmetric with the electric energy of the matrix larger than the droplet. In contrast to the thermodynamic formulation $-c\nabla\mu$, the surface tension force has also been written as $\gamma K\delta$ [29,30], where γ and K are respectively the surface tension and the mean curvature. This formulation is motivated by the Young-Laplace equation by distributing the fluid static pressure γK into a finite interface via an appropriate smooth Delta function δ. The advantage is the direct interpretation of the equilibrium pressure. However, the surface tension γ can vary with time when the interface is not well established, for example, at the early stage of the phase separation. The surface tension is nothing but the excess free energy across the interface. According to this interpretation, the formulation of the surface tension force in terms of the chemical potential is more generalized than a constant value of the surface tension. In this work, the thermodynamic formulation for the surface tension will be extended when an electric field is present to account for the dielectric and Coulomb forces.

These state-of-the-art EHD models are all based on the great route explored by the fluid mechanic society, which mainly focuses on the electrohydrodynamic dominated fluid flow [6,26,31–33]. In other words, the diffusion process is barely paid attention to and thermodynamics is vastly neglected. However, for applications where surface tension plays a vital role, such as micro-scale droplet coalescence, droplet breakup by electrospinning, electric field enhanced spinodal decomposition, electrowetting/dewetting, the electrochemical potential and the resultant surface tension force in previous models is not rigorously deduced with thermodynamic consistency which shall obey the principle of energy dissipation. Here, we revisit the electrochemical potential expression in our electro-hydro-thermodynamic (EHTD) model and extend it to multi-component systems for both leaky and perfect dielectric materials. We validate our EHTD model with the theory of Taylor [1] and Feng [3] for the binary leaky dielectric system. Furthermore, with the help of the revised electrochemical potential, the underlying mechanism of the electric field thinning/thickening surface tension is discussed from the thermodynamic perspective. In addition, the double droplet coalescence and ternary spinodal decomposition are investigated as exemplary applications.

2. Model

2.1. System definition

In this work, we investigate a multi-component fluid system coupled with hydrodynamics and electrodynamics inside the domain Ω enclosed by the boundary S, as schematically illustrated in Fig. 1. The domain is subjected to an electric field $\mathbf{E}$ with voltages Ψ_1 and Ψ_0 at the top and bottom boundaries, respectively. The electrostatic potential is represented by Ψ. The fluid consists of N components and the space $\boldsymbol{x}$ and time t dependent fluid composition is represented by $\boldsymbol{c} = (c_1, c_2, \dots, c_N)$. The number of the

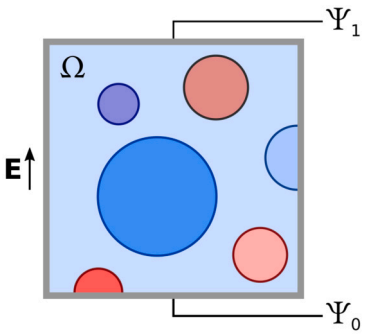

Fig. 1. Schematic of the multicomponent fluid system amid the domain Ω within the electric field **E**. The domain boundary S is colored in gray. The voltages at the top and bottom boundaries are Ψ_1 and Ψ_0, respectively. (For interpretation of the colors in the figure(s), the reader is referred to the web version of this article.)

immiscible phases in the N-component system depends on the formulation of the chemical free energy $\mathcal{F}$. The density of the fluid $\rho(\boldsymbol{x})$ does not vary with time within the scope of incompressible fluids. The convection velocity is denoted by $\mathbf{u}$. The charge density is denoted by $\rho_e(\boldsymbol{x},t)$. The system is at a constant temperature and one atmosphere pressure. No mass and heat in-/outflow are considered at the boundaries of the domain. The system energy functional $\mathcal{L}$ is spatial and temporal dependent and consists of three main parts, namely, the chemical free energy functional $\mathcal{F}$, the macroscopic kinetic energy $\mathcal{K}$, and the electric energy functional $\mathcal{U}$

$$\mathcal{L} = \mathcal{F}(\boldsymbol{x},t,\boldsymbol{c},\nabla\boldsymbol{c}) + \mathcal{K}(\boldsymbol{x},t,\rho,\mathbf{u}) + \mathcal{U}(\boldsymbol{x},t,\rho_e,\nabla\Psi).$$

Other notations applied for the model description are documented in Appendix A.

2.2. Chemical free energy functional $\mathcal{F}$

The chemical free energy functional of mixture $\mathcal{F}$ in the domain Ω is formulated as the summation of the bulk free energy density $f(\boldsymbol{c})$ and the gradient-related interfacial term as

$$\mathcal{F} = \int_\Omega g(\boldsymbol{c},\nabla\boldsymbol{c})\,\mathrm{d}\Omega = \int_\Omega \Big[f(\boldsymbol{c}) + \sum_{i=1}^{N} \frac{\kappa\,\epsilon}{2}\big(\nabla c_i\big)^2\Big]\mathrm{d}\Omega. \tag{1}$$

The interfacial tension parameter κ and the interface width parameter ϵ jointly scale the surface tension. Here, we adopt the regular solution model for f as

$$f(\boldsymbol{c}) = \frac{R_g T}{v_m}\Big(\sum_{i=1}^{N} c_i \ln c_i + \sum_{i<j}^{N,N} \chi_{ij}\, c_i c_j + \sum_{i<j<k}^{N,N,N} \chi_{ijk}\, c_i c_j c_k\Big), \tag{2}$$

in which the molecular interaction between components is quantified by the Flory parameter χ_{ij}, as $\chi_{ij} > 0$ denotes the repulsion and vice versa [34]. The triple interaction is scaled by χ_{ijk}. The gas constant, temperature, and molar volume are represented by R_g, T, and v_m, respectively. At equilibrium, the interfacial tension γ^* between the droplet and matrix without the external electric field is calculated as

$$\gamma^* = \int_{c_m}^{c_d} \sqrt{\kappa\,\epsilon\Delta f}\,\mathrm{d}c = \int_0^\infty \sum_{i=1}^{N} \kappa\,\epsilon\,(\nabla c_i)^2\,\mathrm{d}x, \tag{3}$$

where the equilibrium concentrations of the matrix and droplet are labeled as $\mathbf{c}_m$ and $\mathbf{c}_d$, respectively [35,36]. The excessive free energy density Δf is defined as $f(\mathbf{c}) - f(\mathbf{c}_m) - (\partial f/\partial\mathbf{c} - \kappa\,\epsilon\nabla^2\mathbf{c})\cdot(\mathbf{c}-\mathbf{c}_m)$.

2.3. Kinetic energy $\mathcal{K}$

The kinetic energy takes the following formulation with the constant density ρ and the macroscopic fluid flow velocity $\mathbf{u}$

$$\mathcal{K} = \int_\Omega \frac{\rho\,\mathbf{u}^2}{2}\,\mathrm{d}\Omega. \tag{4}$$

2.4. Electric potential energy $\mathcal{U}$

The electric potential energy $\mathcal{U}$ is considered when the system is placed inside an electrostatic field

$$\mathcal{U} = \int_\Omega u(\rho_e,\nabla\Psi)\,\mathrm{d}\Omega = \int_\Omega \Big[-\frac{\epsilon}{2}(\nabla\Psi)^2 + \rho_e\,\Psi\Big]\mathrm{d}\Omega. \tag{5}$$

The volume integral in Eq. (5) is composed of two aspects. One stems from the energy density of the electric field related to the material permittivity $\varepsilon = \sum_{i=1}^{N} \varepsilon_i c_i$ with ε_i representing the permittivity of component i. The other term $\rho_e \Psi$ denotes the energy needed for putting the charge ρ_e onto the electric potential Ψ. For perfect dielectric systems where no charge exists, this term can be canceled. By applying the Gauss' law $\nabla \cdot (\varepsilon \nabla \Psi) = -\rho_e$ and the divergence theorem, together with the no-flux boundary condition on the boundary S, the electrostatic energy functional can be rewritten as

$$\mathcal{U} = \int_{\Omega} \Big[-\frac{\varepsilon}{2} (\nabla \Psi)^2 - \nabla \cdot (\varepsilon \Psi \nabla \Psi) + \varepsilon (\nabla \Psi)^2 \Big] \mathrm{d}\Omega = \int_{\Omega} \frac{\varepsilon}{2} (\nabla \Psi)^2 \mathrm{d}\Omega.$$

2.5. Electrochemical potential

With the above total energy functional, we define the electrochemical potential μ_i of the component i as the functional derivative of $\mathcal{L}$ with respect to the concentration c_i. The electrochemical potential is composed of two aspects, namely, the contributions from the chemical free energy density $\delta g / \delta c_i$ and the electric energy density $\delta u / \delta c_i$

$$\mu_i = \frac{\delta g}{\delta c_i} + \frac{\delta u}{\delta c_i} = \frac{\partial f}{\partial c_i} - \kappa \epsilon \nabla^2 c_i - \frac{1}{2} \frac{\partial \varepsilon}{\partial c_i} \big(\nabla \Psi \big)^2. \tag{6}$$

3. Energy law

Abiding by the second law of thermodynamics, the total energy functional $\mathcal{L}$ ought to dissipate as

$$\mathrm{d}\mathcal{L} / \mathrm{d}t \leq 0,$$

at any time t for the whole system Ω. To prove this energy-minimizing principle, we decompose the total dissipation into three components.

3.1. Chemical free energy functional dissipation

The time derivative of the free energy functional of mixture $\mathcal{F}$ is deduced with the definition of the materials derivative and the calculus of derivative

$$\frac{\mathrm{d}\nabla c_i}{\mathrm{d}t} = \frac{\partial \nabla c_i}{\partial t} + \mathbf{u} \cdot \nabla \nabla c_i, \quad \frac{\partial \nabla c_i}{\partial t} = \nabla \frac{\partial c_i}{\partial t}. \tag{7}$$

By using Eq. (7), the total derivative of the chemical free energy functional is derived as

$$\begin{aligned}
\frac{\mathrm{d}\mathcal{F}}{\mathrm{d}t} &= \int_{\Omega} \frac{\mathrm{d}g(\boldsymbol{c}, \nabla \boldsymbol{c})}{\mathrm{d}t} \mathrm{d}\Omega \\
&= \int_{\Omega} \sum_{i=1}^{N} \Big[\frac{\partial g}{\partial c_i} \frac{\mathrm{d}c_i}{\mathrm{d}t} + \frac{\partial g}{\partial \nabla c_i} \cdot \frac{\mathrm{d}(\nabla c_i)}{\mathrm{d}t} \Big] \mathrm{d}\Omega \\
&= \int_{\Omega} \sum_{i=1}^{N} \Big[\frac{\partial f}{\partial c_i} \frac{\mathrm{d}c_i}{\mathrm{d}t} + \kappa \epsilon \nabla c_i \cdot \frac{\mathrm{d}(\nabla c_i)}{\mathrm{d}t} \Big] \mathrm{d}\Omega \\
&= \int_{\Omega} \sum_{i=1}^{N} \Big[\frac{\partial f}{\partial c_i} \frac{\mathrm{d}c_i}{\mathrm{d}t} + \kappa \epsilon \nabla c_i \cdot \nabla (\partial_t c_i) + \kappa \epsilon \nabla c_i \cdot \mathbf{u} \cdot \nabla \nabla c_i \Big] \mathrm{d}\Omega \\
&= \int_{\Omega} \sum_{i=1}^{N} \Big[\Big(\frac{\partial f}{\partial c_i} - \kappa \epsilon \nabla^2 c_i \Big) \frac{\mathrm{d}c_i}{\mathrm{d}t} + \kappa \epsilon \nabla^2 c_i \left(\mathbf{u} \cdot \nabla c_i \right) + \kappa \epsilon \nabla c_i \cdot \mathbf{u} \cdot \nabla \nabla c_i \Big] \mathrm{d}\Omega.
\end{aligned}$$

By using a well-known equality of vector calculus, $\nabla \cdot (\mathbf{a} \otimes \mathbf{b}) = (\nabla \cdot \mathbf{a}) \mathbf{b} + \mathbf{a} \cdot \nabla \mathbf{b}$, the above equation is further simplified as

$$\begin{aligned}
\frac{d\mathcal{F}}{\mathrm{d}t} &= \int_{\Omega} \sum_{i=1}^{N} \Big[\Big(\frac{\partial f}{\partial c_i} - \kappa \epsilon \nabla^2 c_i \Big) \frac{\mathrm{d}c_i}{\mathrm{d}t} + \nabla \cdot \left(\kappa \epsilon \nabla c_i \otimes \nabla c_i \right) \cdot \mathbf{u} \Big] \mathrm{d}\Omega \\
&= \int_{\Omega} \sum_{i=1}^{N} \Big[\frac{\delta g}{\delta c_i} \frac{\mathrm{d}c_i}{\mathrm{d}t} + \nabla \cdot \big(\frac{\partial g}{\partial \nabla c_i} \otimes \nabla c_i \big) \cdot \mathbf{u} \Big] \mathrm{d}\Omega.
\end{aligned} \tag{8}$$

With this derivation, we obtain the definition of the chemical potential $\delta g / \delta c_i$. The formulation of the chemical potential is consistent with the variational calculus as well as the Euler-Lagrange equation. The rest term is consistent with the Kortweg stress tensor $\nabla c_i \otimes \nabla c_i$ by using the relation $\partial g / \partial \nabla c_i \sim \nabla c_i$ if Cahn's formulation for the free energy is applied. This term is responsible for the transformation of the free energy into the macroscopic kinetic energy, $\rho \mathbf{u}^2 / 2$. The combination of the Kortweg stress tensor with the grand potential leading to the thermodynamic formulation of the surface tension force, as will be demonstrated in Sec. 5.

3.2. Electric energy functional dissipation

The time derivative of the electric energy functional $\mathcal{U}$ is categorized into two cases: (I) and (II).

(I) For the leaky dielectric system with net charges, the charge density ρ^e evolves with time. The net charge can be induced by the electric field. In this way, we derive the time derivative of the electric energy functional as

$$\begin{aligned}\frac{\mathrm{d}\mathcal{U}}{\mathrm{d}t} &= \int_\Omega \frac{\mathrm{d}}{\mathrm{d}t}\left[\rho_e \Psi - \frac{\varepsilon}{2}(\nabla\Psi)^2\right]\mathrm{d}\Omega \\ &= \int_\Omega \left[\Psi\frac{\mathrm{d}\rho_e}{\mathrm{d}t} + \rho_e\frac{\mathrm{d}\Psi}{\mathrm{d}t} - \sum_{i=1}^{N}\frac{1}{2}\frac{\partial\varepsilon}{\partial c_i}(\nabla\Psi)^2\frac{\mathrm{d}c_i}{\mathrm{d}t} - \varepsilon\nabla\Psi\cdot\frac{\mathrm{d}(\nabla\Psi)}{\mathrm{d}t}\right]\mathrm{d}\Omega \\ &= \int_\Omega \left[\Psi\frac{\mathrm{d}\rho_e}{\mathrm{d}t} + \rho_e\frac{\mathrm{d}\Psi}{\mathrm{d}t} - \sum_{i=1}^{N}\frac{\mathbf{E}^2}{2}\frac{\partial\varepsilon}{\partial c_i}\cdot\frac{\mathrm{d}c_i}{\mathrm{d}t} - \nabla\cdot\left(\varepsilon\mathbf{E}\right)\frac{\mathrm{d}\Psi}{\mathrm{d}t} - \nabla\cdot(\varepsilon\mathbf{E}\otimes\mathbf{E})\cdot\mathbf{u}\right]\mathrm{d}\Omega \qquad (9)\\ &= \int_\Omega \left[\frac{\delta u}{\delta\rho_e}\frac{\mathrm{d}\rho_e}{\mathrm{d}t} + \sum_{i=1}^{N}\frac{\delta u}{\delta c_i}\frac{\mathrm{d}c_i}{\mathrm{d}t} - \nabla\cdot\left(\frac{\partial u}{\partial\nabla\Psi}\otimes\nabla\Psi\right)\cdot\mathbf{u}\right]\mathrm{d}\Omega. \qquad (10)\end{aligned}$$

Here, Gauss' law is used to cancel the second term with the fourth term in Eq. (9).

(II) For the perfect dielectric system, there is no net charge. The electrostatic functional only contains the gradient of the electrostatic potential. By using the vector calculus, $\nabla\cdot(\mathbf{a}\otimes\mathbf{b}) = (\nabla\cdot\mathbf{a})\mathbf{b} + \mathbf{a}\cdot\nabla\mathbf{b}$, and the total derivative of gradient-term related function, we obtain the following equation

$$\begin{aligned}\frac{\mathrm{d}\mathcal{U}}{\mathrm{d}t} &= \int_\Omega \frac{\mathrm{d}}{\mathrm{d}t}\left[-\frac{\varepsilon}{2}(\nabla\Psi)^2\right]\mathrm{d}\Omega \\ &= \int_\Omega \left[-\sum_{i=1}^{N}\frac{(\nabla\Psi)^2}{2}\frac{\partial\varepsilon}{\partial c_i}\frac{\mathrm{d}c_i}{\mathrm{d}t} - \nabla\cdot(\varepsilon\nabla\Psi\otimes\nabla\Psi)\cdot\mathbf{u}\right]\mathrm{d}\Omega \\ &= \int_\Omega \left[\sum_{i=1}^{N}\frac{\delta u}{\delta c_i}\frac{\mathrm{d}c_i}{\mathrm{d}t} - \nabla\cdot\left(\frac{\partial u}{\partial\nabla\Psi}\otimes\nabla\Psi\right)\cdot\mathbf{u}\right]\mathrm{d}\Omega. \qquad (11)\end{aligned}$$

Note that both Eq. (10) and Eq. (11) lead to a term $\sim\nabla\Psi\otimes\nabla\Psi$ if $u\sim(\nabla\Psi)^2$ is applied. This new term is consistent with the Maxwell stress tensor. As the effect of the chemical term $\nabla c_i\otimes\nabla c_i$, the stress tensor $\nabla\Psi\otimes\nabla\Psi$ is responsible for the transformation of the electrostatic energy into the kinetic energy.

3.3. Kinetic energy dissipation

The kinetic energy evolution is governed by the Navier-Stokes equations

$$\nabla\cdot\mathbf{u} = 0, \qquad (12)$$

$$\rho\frac{\mathrm{d}\mathbf{u}}{\mathrm{d}t} = \nabla\cdot(-p\mathbf{I} + \underline{\underline{\mathrm{T}}} - \underline{\underline{\Theta}} - \underline{\underline{\sigma}}^{\mathrm{M}}), \qquad (13)$$

where p stands for the hydrodynamic pressure solved by the incompressibility condition via $\nabla\cdot\mathbf{u} = 0$. The viscous stress tensor $\underline{\underline{\mathrm{T}}}$, thermodynamic stress tensor $\underline{\underline{\Theta}}$, and electrostatic Maxwell stress tensor $\underline{\underline{\sigma}}^{\mathrm{M}}$ are formulated as

$$\begin{aligned}\underline{\underline{\mathrm{T}}} &= \eta\left(\nabla\mathbf{u} + \nabla\mathbf{u}^T\right), \\ \underline{\underline{\Theta}} &= -\left(g - \sum_{i=1}^{N}\frac{\delta g}{\delta c_i}c_i\right)\mathbf{I} + \sum_{i=1}^{N}\frac{\partial g}{\partial\nabla c_i}\otimes\nabla c_i, \\ \underline{\underline{\sigma}}^{\mathrm{M}} &= -\left(u - \sum_{i=1}^{N}\frac{\delta u}{\delta c_i}c_i - \frac{\delta u}{\delta\rho_e}\rho_e\right)\mathbf{I} - \frac{\partial u}{\partial\nabla\Psi}\otimes\nabla\Psi.\end{aligned}$$

With the assumption that the density does not change with time, the kinetic energy of the whole system $\mathcal{K}$ dissipates as

$$\begin{aligned}\frac{\mathrm{d}\mathcal{K}}{\mathrm{d}t} &= \int_\Omega \rho\frac{\mathrm{d}\mathbf{u}}{\mathrm{d}t}\cdot\mathbf{u}\,\mathrm{d}\Omega \\ &= \int_\Omega \nabla\cdot\left[-P\mathbf{I} - \sum_{i=1}^{N}\frac{\partial g}{\partial\nabla c_i}\otimes\nabla c_i + \frac{\partial u}{\partial\nabla\Psi}\otimes\nabla\Psi + \eta\left(\nabla\mathbf{u} + \nabla\mathbf{u}^T\right)\right]\cdot\mathbf{u}\,\mathrm{d}\Omega. \qquad (14)\end{aligned}$$

Here, in contrast to the thermodynamic potential, we define a generalized grand potential P as

$$P = p - g - u + \sum_{i=1}^{N}\Big(\frac{\delta g}{\delta c_i}c_i + \frac{\delta u}{\delta c_i}c_i\Big) + \frac{\delta u}{\delta \rho_e}\rho_e$$
$$= p - g - u + \sum_{i=1}^{N}\mu_i c_i + \rho_e\Psi. \tag{15}$$

Considering the no-slip boundary condition and the incompressibility assumption with $\nabla\cdot\mathbf{u}=0$, it is noteworthy that

$$\int_{\Omega} -\nabla\cdot(P\,\mathbf{I})\cdot\mathbf{u}\,\mathrm{d}\Omega = 0.$$

Substituting Eq. (15) into Eq. (14), the kinetic energy dissipation follows

$$\frac{\mathrm{d}\,\mathcal{K}}{\mathrm{d}\,t} = \int_{\Omega}\nabla\cdot\Big[-\sum_{i=1}^{N}\frac{\partial g}{\partial\nabla c_i}\otimes\nabla c_i + \frac{\partial u}{\partial\nabla\Psi}\otimes\nabla\Psi + \eta\big(\nabla\mathbf{u}+\nabla\mathbf{u}^T\big)\Big]\cdot\mathbf{u}\,\mathrm{d}\Omega. \tag{16}$$

3.4. Total energy functional dissipation

Next, we derive the evolution equations for the composition $\boldsymbol{c}$ and the charge density ρ^e by considering the dissipation of the system energy. Combining Eq. (8), Eq. (10) and Eq. (16), the total energy functional of the *leaky dielectric system* dissipates with time as

$$\frac{\mathrm{d}\,\mathcal{L}}{\mathrm{d}\,t} = \int_{\Omega}\Big\{\nabla\cdot\Big[\eta\big(\nabla\mathbf{u}+\nabla\mathbf{u}^T\big)\Big]\cdot\mathbf{u} + \sum_{i=1}^{N}\Big(\frac{\delta g}{\delta c_i}+\frac{\delta u}{\delta c_i}\Big)\frac{\mathrm{d}c_i}{\mathrm{d}t} + \frac{\delta u}{\delta\rho_e}\frac{\mathrm{d}\rho_e}{\mathrm{d}t}\Big\}\,\mathrm{d}\Omega$$
$$= \int_{\Omega}\Big\{\nabla\cdot\Big[\eta\big(\nabla\mathbf{u}+\nabla\mathbf{u}^T\big)\Big]\cdot\mathbf{u} + \sum_{i=1}^{N}\mu_i\frac{\mathrm{d}c_i}{\mathrm{d}t} + \Psi\frac{\mathrm{d}\rho_e}{\mathrm{d}t}\Big\}\,\mathrm{d}\Omega.$$

Obviously, the dissipation of $\mathcal{L}$ is decided by choosing the time evolution equations for the composition $\boldsymbol{c}$, and the charge density ρ_e. Here, we adopt the conservation equation for the charge density and take the charge convection and relaxation both into consideration as

$$\frac{\partial\rho_e}{\partial t} + \nabla\cdot(\mathbf{u}\,\rho_e) = \nabla\cdot(\sigma\nabla\Psi).$$

The material conductivity is expressed as $\sigma = \sum_{i=1}^{N}\sigma_i c_i$ with σ_i representing the conductivity of component i.

For the composition evolution, two feasible options are available, namely,

(I) Cahn-Hilliard model, which is a kind of diffusion equation

$$\frac{\mathrm{d}c_i}{\mathrm{d}t} = \nabla\cdot\Big(\sum_{j=1}^{N}\mathcal{M}_{ij}\nabla\mu_j\Big),$$

which is derived with the Gibbs-Duhem equation for the multicomponent system [37]. The mobility $\mathcal{M}$ is a $N\times N$ positive semi-definite matrix for arbitrary values of the gradient of the chemical potential. In some works, the constant mobility $\mathcal{M}_0$ is adopted with $\mathcal{M}_0 = \sum_{i=1}^{N}D_i c_i$ and D_i stands for the diffusivity of component i [38–40]. Another classic formulation is proposed by Onsager with the reciprocal relation as $\mathcal{M}_{ij} = \mathcal{M}_0\,c_i(\delta_{ij}-c_j)$ [41,42]; a detailed derivation based on the Gibbs-Duhem relation is shown in Ref. [37].

(II) Allen-Cahn model, a type of reaction equation [43–46]

$$\frac{\mathrm{d}c_i}{\mathrm{d}t} = -\tau_i\,\mu_i + \lambda,$$

where τ_i is the kinetic parameter that controls the system evolution speed towards the equilibrium. The Lagrange multiplier λ ensures the constraint $\sum_{i=1}^{N}c_i = 1$ for the N-component system by taking the following formulation

$$\lambda = \frac{1}{N}\sum_{i=1}^{N}\tau_i\,\mu_i. \tag{17}$$

Similarly, combining Eq. (8), Eq. (11), and Eq. (16), the total energy functional of the *perfect dielectric system* evolves with time as

$$\frac{\mathrm{d}\,\mathcal{L}}{\mathrm{d}\,t} = \int_{\Omega}\Big\{\nabla\cdot\Big[\eta\big(\nabla\mathbf{u}+\nabla\mathbf{u}^T\big)\Big]\cdot\mathbf{u} + \sum_{i=1}^{N}\mu_i\frac{\mathrm{d}c_i}{\mathrm{d}t}\Big\}\,\mathrm{d}\Omega.$$

3.4.1. Cahn-Hilliard-Navier-Stokes-Gauss model (CHNSG)

On one hand, substituting the evolution equations for the composition and the charge density, the energy law of the *leaky dielectric system* reads

$$\frac{\mathrm{d}\mathcal{L}}{\mathrm{d}t} = -\int_{\Omega}\Big[\eta\nabla\mathbf{u}:\nabla\mathbf{u} + \sum_{i=1,j=1}^{N,N}\nabla\mu_i\cdot(\mathcal{M}_{ij}\nabla\mu_j) + \sigma\big(\nabla\Psi\big)^2\Big]\mathrm{d}\Omega$$

$$= -\int_{\Omega}\Big[\eta\nabla\mathbf{u}:\nabla\mathbf{u} + \sigma\big(\nabla\Psi\big)^2\Big]\mathrm{d}\Omega - \int_{\Omega^*}\sum_{i=1}^{N}\mathbf{M}_{ii}\big(\nabla^*\mu_i\big)^2\mathrm{d}\Omega^* \le 0.$$

Because the mobility matrix $\mathcal{M}$ is positive semi-definite, we define the gradient operator $\nabla^* := \mathbf{L}\nabla$ in the Ω^* space. The transformation matrix $\mathbf{L}$ is reckoned with the Cholesky decomposition of $\mathcal{M} = \mathbf{L}^T\mathbf{M}\mathbf{L}$.

On the other hand, the energy law of the *perfect dielectric system* reads

$$\frac{\mathrm{d}\mathcal{L}}{\mathrm{d}t} = -\int_{\Omega}\eta\nabla\mathbf{u}:\nabla\mathbf{u}\,\mathrm{d}\Omega - \int_{\Omega^*}\sum_{i=1}^{N}\mathbf{M}_{ii}\big(\nabla^*\mu_i\big)^2\mathrm{d}\Omega^* \le 0.$$

3.4.2. Allen-Cahn-Navier-Stokes-Gauss model (ACNSG)

For leaky dielectric systems, the total energy functional $\mathcal{L}$ dissipates as

$$\frac{\mathrm{d}\mathcal{L}}{\mathrm{d}t} = -\int_{\Omega}\Big[\eta\nabla\mathbf{u}:\nabla\mathbf{u} + \sum_{i=1}^{N}\tau_i\,\mu_i^2 + \sigma\big(\nabla\Psi\big)^2\Big]\mathrm{d}\Omega \le 0.$$

For the perfect dielectric system, we have

$$\frac{\mathrm{d}\mathcal{L}}{\mathrm{d}t} = -\int_{\Omega}\Big[\eta\nabla\mathbf{u}:\nabla\mathbf{u} + \sum_{i=1}^{N}\tau_i\,\mu_i^2\Big]\mathrm{d}\Omega \le 0.$$

4. Grand pressure and curvature effect

Considering a droplet with a radius R inside a domain, the chemical potential in the entire domain reaches the equilibrium μ_i^e which is expressed in d-dimensional polar coordinate ($d = 2,\ 3$) as

$$\mu_i^e = \frac{\delta g}{\delta c_i} + \frac{\delta u}{\delta c_i} = \frac{\partial f}{\partial c_i} - \kappa\,\epsilon\Big(\frac{\partial^2 c_i}{\partial r^2} + \frac{d-1}{r}\frac{\partial c_i}{\partial r}\Big) - \frac{1}{2}\frac{\partial\varepsilon}{\partial c_i}\big(\nabla\Psi\big)^2.$$

Multiplying by $\partial c_i/\partial r$ and integrating from 0 (droplet center) to ∞, and summing the equations for different components yield

$$\begin{aligned}
&\int_0^{\infty}\sum_{i=1}^{N}\mu_i^e\frac{\partial c_i}{\partial r}\,\mathrm{d}r\\
&= \int_0^{\infty}\sum_{i=1}^{N}\Big[\frac{\partial f}{\partial c_i} - \frac{1}{2}\frac{\partial\varepsilon}{\partial c_i}\big(\nabla\Psi\big)^2 - \kappa\,\epsilon\Big(\frac{\partial^2 c_i}{\partial r^2} + \frac{d-1}{r}\frac{\partial c_i}{\partial r}\Big)\Big]\frac{\partial c_i}{\partial r}\mathrm{d}r\\
&= \int_0^{\infty}\sum_{i=1}^{N}\Big[\frac{\partial f}{\partial c_i} - \kappa\,\epsilon\Big(\frac{\partial^2 c_i}{\partial r^2} + \frac{d-1}{r}\frac{\partial c_i}{\partial r}\Big)\Big]\frac{\partial c_i}{\partial r}\mathrm{d}r - \int_0^{\infty}\frac{1}{2}\frac{\partial\varepsilon}{\partial r}\big(\nabla\Psi\big)^2\mathrm{d}r\\
&= \Big[f(\boldsymbol{c}) + \sum_{i=1}^{N}\frac{\kappa\,\epsilon}{2}\big(\nabla c_i\big)^2\Big]\Big|_0^{\infty} - \frac{d-1}{r}\int_0^{\infty}\sum_{i=1}^{N}\kappa\,\epsilon\Big(\frac{\partial c_i}{\partial r}\Big)^2\mathrm{d}r - \int_0^{\infty}\frac{1}{2}\frac{\partial\varepsilon}{\partial r}\big(\nabla\Psi\big)^2\mathrm{d}r\\
&= g(\boldsymbol{c},\nabla\boldsymbol{c})\Big|_0^{\infty} - \frac{d-1}{r}\int_0^{\infty}\sum_{i=1}^{N}\kappa\,\epsilon\Big(\frac{\partial c_i}{\partial r}\Big)^2\mathrm{d}r - \int_0^{\infty}\frac{1}{2}\frac{\partial\varepsilon}{\partial r}\big(\nabla\Psi\big)^2\mathrm{d}r.
\end{aligned}\tag{18}$$

By applying the integration by parts, we rewrite the last integral in Eq. (18)

$$\begin{aligned}
\int_0^{\infty}\frac{1}{2}\frac{\partial\varepsilon}{\partial r}\big(\nabla\Psi\big)^2\mathrm{d}r &= \frac{\varepsilon}{2}\big(\nabla\Psi\big)^2\Big|_0^{\infty} - \int_0^{\infty}\varepsilon\frac{\partial\Psi}{\partial r}\nabla^2\Psi\mathrm{d}r\\
&= \frac{\varepsilon}{2}\big(\nabla\Psi\big)^2\Big|_0^{\infty} - \int_0^{\infty}\varepsilon\Big[\frac{d-1}{r}\Big(\frac{\partial\Psi}{\partial r}\Big)^2 + \frac{\partial\Psi}{\partial r}\frac{\partial^2\Psi}{\partial r^2}\Big]\mathrm{d}r\\
&= \frac{\varepsilon}{2}\big(\nabla\Psi\big)^2\Big|_0^{\infty} - \int_0^{\infty}\frac{d-1}{r}\varepsilon\Big(\frac{\partial\Psi}{\partial r}\Big)^2\mathrm{d}r - \int_0^{\infty}\varepsilon\frac{\partial\Psi}{\partial r}\mathrm{d}\Big(\frac{\partial\Psi}{\partial r}\Big)
\end{aligned}$$

$$= \frac{\varepsilon}{2}\left(\nabla\Psi\right)^2\Big|_0^\infty - \int_0^\infty \frac{d-1}{r}\varepsilon\left(\frac{\partial\Psi}{\partial r}\right)^2 \mathrm{d}r - \varepsilon\left(\frac{\partial\Psi}{\partial r}\right)^2\Big|_0^\infty$$

$$= \frac{\varepsilon}{2}\left(\nabla\Psi\right)^2\Big|_0^\infty - \int_0^\infty \frac{d-1}{r}\varepsilon\left(\frac{\partial\Psi}{\partial r}\right)^2 \mathrm{d}r. \tag{19}$$

Substituting Eq. (19) into Eq. (18), we have

$$\begin{aligned}
&\int_0^\infty \sum_{i=1}^N \mu_i^e \frac{\partial c_i}{\partial r}\,\mathrm{d}r \\
&= \left[g(\boldsymbol{c},\nabla\boldsymbol{c}) - \frac{\varepsilon}{2}\left(\nabla\Psi\right)^2\right]\Big|_0^\infty - \int_0^\infty (d-1)\left[\sum_{i=1}^N \frac{\kappa\,\epsilon}{r}\left(\frac{\partial c_i}{\partial r}\right)^2 - \frac{\varepsilon}{r}\left(\frac{\partial\Psi}{\partial r}\right)^2\right]\mathrm{d}r \\
&= \left(g + u - \rho_e\Psi\right)\Big|_0^\infty - \int_0^\infty (d-1)\left[\sum_{i=1}^N \frac{\kappa\,\epsilon}{r}\left(\frac{\partial c_i}{\partial r}\right)^2 - \frac{\varepsilon}{r}\left(\frac{\partial\Psi}{\partial r}\right)^2\right]\mathrm{d}r \\
&= \sum_{i=1}^N \left(\mu^e c_i\right)\Big|_0^\infty.
\end{aligned}$$

At equilibrium, with the formulation of the grand pressure P in Eq. (15), the curvature effect on the pressure ΔP with the first-order approximation is replicated as

$$\begin{aligned}
\Delta P = P(0) - P(\infty) &= \left(g + u - \rho_e\Psi - \sum_{i=1}^N \mu_i^e c_i\right)\Big|_0^\infty \\
&= \int_0^\infty (d-1)\left[\sum_{i=1}^N \frac{\kappa\,\epsilon}{r}\left(\frac{\partial c_i}{\partial r}\right)^2 - \frac{\varepsilon}{r}\left(\frac{\partial\Psi}{\partial r}\right)^2\right]\mathrm{d}r \\
&= \frac{(d-1)\,\gamma}{R} + \mathcal{O}\left(\frac{1}{R^2}\right),
\end{aligned}$$

in which R represents the droplet radius and the surface tension γ reads

$$\gamma = \int_0^\infty \left[\sum_{i=1}^N \kappa\,\epsilon\left(\frac{\partial c_i}{\partial r}\right)^2 - \varepsilon\left(\frac{\partial\Psi}{\partial r}\right)^2\right]\mathrm{d}r. \tag{20}$$

5. Forces

In the Navier-Stokes equation, Eq. (13), the complex divergence of the surface stress tensor $\underline{\underline{\Theta}}$ and electrostatic Maxwell stress tensor $\underline{\underline{\sigma}}^{\mathrm{M}}$ can be simplified as the thermodynamic force $\boldsymbol{f}_c$ and the dielectric force $\boldsymbol{f}_e$, respectively. We find that these force terms can be simplified as

(I) The thermodynamic force

$$\begin{aligned}
\boldsymbol{f}_c = -\nabla\cdot\underline{\underline{\Theta}} &= \nabla\cdot\left[\left(g - \sum_{i=1}^N \frac{\delta g}{\delta c_i}c_i\right)\mathbf{I} - \sum_{i=1}^N \frac{\partial g}{\partial\nabla c_i}\otimes\nabla c_i\right] \\
&= -\sum_{i=1}^N c_i\,\nabla\left(\frac{\delta g}{\delta c_i}\right).
\end{aligned} \tag{21}$$

(II) The dielectric force

$$\begin{aligned}
\boldsymbol{f}_e = \nabla\cdot\underline{\underline{\sigma}}^{\mathrm{M}} &= \nabla\cdot\left[\left(u - \sum_{i=1}^N \frac{\delta u}{\delta c_i}c_i - \frac{\delta u}{\delta\rho_e}\rho_e\right)\mathbf{I} - \frac{\partial u}{\partial\nabla\Psi}\otimes\nabla\Psi\right] \\
&= \nabla\cdot\left\{\left[\rho_e\Psi - \frac{1}{2}\varepsilon(\nabla\Psi)^2 - \sum_{i=1}^N \frac{\delta u}{\delta c_i}c_i - \frac{\delta u}{\delta\rho_e}\rho_e\right]\mathbf{I} - \frac{\partial u}{\partial\nabla\Psi}\otimes\nabla\Psi\right\} \\
&= \sum_{i=1}^N \nabla\left[\frac{c_i}{2}\frac{\partial\varepsilon}{\partial c_i}\left(\nabla\Psi\right)^2\right] - \frac{1}{2}\nabla\varepsilon\left(\nabla\Psi\right)^2 - \rho_e\nabla\Psi
\end{aligned} \tag{22}$$

$$= -\sum_{i=1}^{N} c_i \nabla\Big(\frac{\delta u}{\delta c_i}\Big) - \rho_e \nabla\Big(\frac{\delta u}{\delta \rho_e}\Big). \tag{23}$$

Both $\boldsymbol{f}_e$ and $\boldsymbol{f}_c$ can be written in the tensor format. The force in Eq. (23) consists of two parts. Both of them are expressed in a conservative way, like the force term in Eq. (21). Most importantly, the first term in Eq. (22) is a coupling contribution of the dielectric force by the chemical part. In previous models, this term is interpreted as the electrorestriction force

$$\nabla\Big[\frac{\rho}{2}\frac{\partial \varepsilon}{\partial \rho}\big(\nabla\Psi\big)^2\Big],$$

and is erroneously neglected due to the constant density assumption for one-phase flow or pure fluid dynamics problem. However, for multi-component systems with diffusion, one cannot use density as the variable for the diffusion process. Instead, the permittivity depends on the composition $\boldsymbol{c}$ and varies in space. The second term in Eq. (23) is the regular Coulomb's force by using the relation $\delta u/\delta \rho_e = \Psi$.

6. Evolution equations

6.1. Cahn-Hilliard-Navier-Stokes-Gauss EHTD model

The final **CHNSG** equations for the *leaky dielectric* read

$$\begin{aligned}
&\text{(1) Incompressibility} && \nabla\cdot\mathbf{u} = 0,\\
&\text{(2) Gaussian law} && \nabla\cdot(\varepsilon\nabla\Psi) = -\rho_e,\\
&\text{(3) Charge conservation} && \partial_t\rho_e + \nabla\cdot\big(\mathbf{u}\,\rho_e\big) = \nabla\cdot(\sigma\nabla\Psi),\\
&\text{(4) Material conservation} && \partial_t c_i + \nabla\cdot(\mathbf{u}\,c_i) = \nabla\cdot\big(\textstyle\sum_{j=1}^{N}\mathcal{M}_{ij}\nabla\mu_j + \boldsymbol{\xi}_c\big),\\
&\text{(5) Momentum balance} && \rho\,\mathrm{d}_t\mathbf{u} = -\nabla p - \textstyle\sum_{i=1}^{N} c_i\nabla\mu_i - \rho_e\nabla\Psi + \nabla\cdot\big[\eta\,(\nabla\mathbf{u} + \nabla\mathbf{u}^T)\big].
\end{aligned} \tag{24}$$

For the *perfect dielectric system* where no net charges exist, the above equations can be simplified as

$$\begin{aligned}
\nabla\cdot\mathbf{u} &= 0,\\
\nabla\cdot(\varepsilon\nabla\Psi) &= 0,\\
\partial_t c_i + \nabla\cdot(\mathbf{u}\,c_i) &= \nabla\cdot\big(\textstyle\sum_{j=1}^{N}\mathcal{M}_{ij}\nabla\mu_j + \boldsymbol{\xi}_c\big),\\
\rho\,(\partial_t\mathbf{u} + \mathbf{u}\cdot\nabla\mathbf{u}) &= -\nabla p - \textstyle\sum_{i=1}^{N} c_i\nabla\mu_i + \nabla\cdot\big[\eta\,(\nabla\mathbf{u} + \nabla\mathbf{u}^T)\big].
\end{aligned} \tag{25}$$

Here, the composition noise for each component i is adopted as the crucial trigger for the spinodal decomposition, which follows the fluctuation-dissipation theorem as

$$\big\langle \xi_c, \xi_c' \big\rangle = \frac{2\mathcal{M}_{ii}R_g T}{v_m \Delta t}\nabla^2\delta(\boldsymbol{x} - \boldsymbol{x}')\delta(t - t'), \tag{26}$$

where δ is the Dirac's delta. The noise amplitude $\boldsymbol{\xi}_c$ is decided by the gas constant R_g, temperature T, molar volume v_m, and the time step of the simulation Δt. The thermal noise formulation is derived in the quintessential paper by Hohenberg and Halperin [47]. Its realization in the phase-field model has been intensively discussed in Ref. [48]. The numerical accuracy and stability of the stochastic phase-field model coupled with hydrodynamics have been studied in our previous study [49].

6.2. Allen-Cahn-Navier-Stokes-Gauss EHTD model

The final **ACNSG** equations for the *leaky dielectric* materials read

$$\begin{aligned}
&\text{(1) Incompressibility} && \nabla\cdot\mathbf{u} = 0,\\
&\text{(2) Gaussian law} && \nabla\cdot(\varepsilon\nabla\Psi) = -\rho_e,\\
&\text{(3) Charge conservation} && \partial_t\rho_e + \nabla\cdot\big(\mathbf{u}\,\rho_e\big) = \nabla\cdot(\sigma\nabla\Psi),\\
&\text{(4) Material conservation} && \partial_t c_i + \nabla\cdot(\mathbf{u}\,c_i) = -\tau_i\,\mu_i + \xi_a + \lambda,\\
&\text{(5) Momentum balance} && \rho\,\mathrm{d}_t\mathbf{u} = -\nabla p - \textstyle\sum_{i=1}^{N} c_i\nabla\mu_i - \rho_e\nabla\Psi + \nabla\cdot\big[\eta\,(\nabla\mathbf{u} + \nabla\mathbf{u}^T)\big].
\end{aligned} \tag{27}$$

For the *perfect dielectric system* without induced charges

$$\begin{aligned} \nabla \cdot \mathbf{u} &= 0, \\ \nabla \cdot (\varepsilon \nabla \Psi) &= 0, \\ \partial_t c_i + \nabla \cdot (\mathbf{u}\, c_i) &= -\tau_i\, \mu_i + \xi_a + \lambda, \\ \rho\,(\partial_t \mathbf{u} + \mathbf{u} \cdot \nabla \mathbf{u}) &= -\nabla p - \textstyle\sum_{i=1}^{N} c_i \nabla \mu_i + \nabla \cdot \left[\eta\,(\nabla \mathbf{u} + \nabla \mathbf{u}^T)\right]. \end{aligned} \tag{28}$$

Here, the composition noise amplitude for the component i in the Allen-Cahn equation obeys

$$\left\langle \xi_a, \xi_a' \right\rangle = \frac{2\tau_i R_g T}{v_m \Delta t} \delta(\boldsymbol{x} - \boldsymbol{x}')\delta(t - t'). \tag{29}$$

In the following, we mainly focus on droplet coalescence and fluid phase separation. Therefore, the ACNSG model is only deduced and will not be applied to simulations in the rest part.

7. Numerical stability and verification

In this section, we first present a concise overview of the contemporary state-of-the-art in numerical methodologies for solving the Cahn-Hilliard-Navier-Stokes equation, which decides the dissipative energy law at the discrete level. Substantial efforts have been dedicated to devising robust discretization methods aimed at yielding unconditionally energy-stable schemes. Noteworthy strategies include the utilization of the convex splitting technique [50,51], the invariant energy quadratization approach [52], and the scalar auxiliary variable approach [53,54]. Also, various strategies have been proposed to mitigate computational expenses. Notable among these is the decoupling of the composition field (phase-field) from the fluid velocity field, as comprehensively discussed in Refs. [55–58]. Furthermore, efforts have been directed towards the exploration of numerical techniques tailored for multi-phase flows characterized by various density and viscosity ratios. This investigation encompasses diverse and intricate scenarios, as documented in Refs. [59,60,17,19,61,18]. In this work, the paramount focus lays in the modeling aspect, related to the formulation and conceptualization of the coupling of the phase field and fluid flow field with the electric field. Therefore, the numerical scheme is not the main concern of this work and is briefly present as follows.

We adopt the finite difference method to solve the Cahn-Hilliard-Navier-Stokes-Gauss model Eqs. (24) with the equidistant Cartesian mesh on a staggered grid, where the domain Ω is discretized with $\Delta x = \Delta y = \Delta z$. To treat the convection fluxes in the phase-field equation, the second order weighted upwind scheme is applied, combined with the Lax-Friedrichs method to enhance the numerical stability (see supplementary Sec. I. A). Meanwhile, the incompressible Navier-Stokes equation is solved with Chorin's projection method [62]; see the supplementary Sec. I. B. for more details. In addition, the explicit Euler scheme is used for solving the diffusion-convection equations for the composition and the charge density. To solve the hydrodynamic pressure p in the incompressible Navier-Stokes equation, as well as the electric potential Ψ following Gauss' law, these two Poisson equations are iterated with the conjugate gradient method. The time step Δt for the explicit Euler scheme is chosen according to the von Neumann stability analysis which is documented in the supplementary Sec. I. E.

7.1. Boundary condition

We apply the following boundary conditions to the Cahn-Hilliard-Navier-Stokes-Gauss equations as

- Neumann boundary condition for the composition c_i, charge density ρ_e, and electrochemical potential μ_i for each component i as:

$$\nabla c_i \cdot \mathbf{n} = 0, \quad \nabla \mu_i \cdot \mathbf{n} = 0, \quad \nabla \rho_e \cdot \mathbf{n} = 0.$$

- Dirichlet boundary condition is applied for electric potential Ψ on the top and bottom boundaries, while no-flux boundary condition is added on the other boundaries with

$$\Psi_{\text{top}} = \Psi_1, \quad \Psi_{\text{bottom}} = \Psi_0,$$

while no-flux boundary condition is added on the other sides

$$\nabla \Psi \cdot \mathbf{n} = 0.$$

- No-slip boundary condition is used for the velocity $\mathbf{u}$ on the top and bottom boundaries, while periodic boundary condition is added on the other boundaries.

$$\mathbf{u}_{\text{top}} = \mathbf{u}_{\text{bottom}} = \mathbf{0},$$

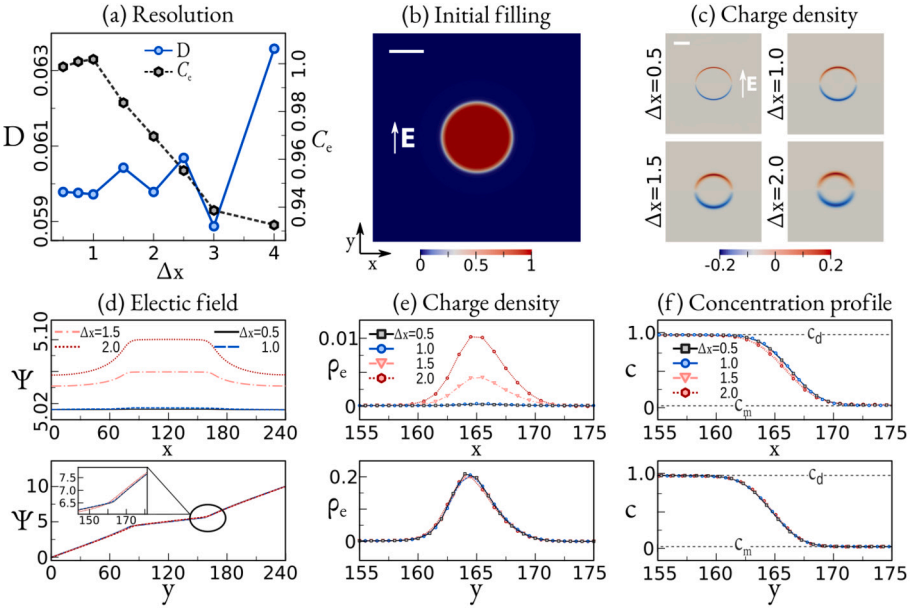

Fig. 2. (a) The verification with the mesh resolution Δx. Blue dots: deformation factor D with Δx; black hexagons: surface charge density C_e with Δx. (b) Initial filling of the red droplet inside the blue matrix. The scale bar denotes 40 and the colorbar measures the droplet concentration. (c) Charge density ρ_e at $t = 1e4$ scaled by the colorbar below. (d) (e) and (f) illustrate the electric potential Ψ, charge density ρ_e, and droplet concentration c at $t = 1e4$ in x and y directions, respectively.

7.2. Mesh resolution Δx

In the first part, we present the numerical stability of our model and vary the resolution by changing Δx from 0.5 to 4.0. The initial simulation setup is illustrated in Fig. 2(b) in which a droplet with the equilibrium composition $c_m = 0.973$ and diameter $d_0 = 80$ is placed amid a 240×240 fluid matrix with the equilibrium composition $c_d = 0.027$; see Fig. 2(b). The electric potential in the domain takes $\Psi_1 = 10$ at the boundary top and $\Psi_0 = 0$ at the bottom. The conductivity σ of the droplet and matrix are chosen as 5.0 and 1.0, respectively, while their permittivities ε are assigned to be 80.0 and 1.0. The Flory parameter in Eq. (2) is fixed as $\chi = 3.78$, with the surface parameter $\kappa = 1.0$ and $\epsilon = 4.0$. The density and viscosity of both droplet and matrix are set to be 1.0. After the non-dimensionalization process (see supplementary), we adopt the following non-dimensionalized number, namely, the Péclet number Pé, Weber number We, Reynold number Re, and electro-capillary number Ca_E in the simulations as

$$\text{Pé} = 1.0, \quad \text{We} = 1.0, \quad \text{Re} = 1.0, \quad \mathrm{Ca}_E = 1.0.$$

For the solution of the incompressible Navier-Stokes equation and Poisson equation, we select the residual threshold eps $= 1e-7$ and simulation timestep $\Delta t = 1e-4$ for the numerical accuracy, which will be discussed in the next part.

Here, two criteria are available for the evaluation process, namely the deformation factor D and the surface charge C_e. The deformation factor reflects the oval shape of the droplet inside the electric field. Fitting the droplet interface with an ellipse, D is calculated as

$$D = \frac{a-b}{a+b}, \tag{30}$$

where a and b represent the lengths of the semi-major axis (align with the x-axis) and the semi-minor axis (the y-axis), respectively. In the diffuse interface phase-field model, the droplet interface position denotes the location with $c = 0.5$, based on which a and b are fitted with the least squares method. The surface charge density C_e is integrated by the charge density ρ_e along the y-axis of the oval droplet from the center as

$$C_e = \int_{Ny/2}^{Ny} \rho_e \, \mathrm{d}y. \tag{31}$$

As shown in Fig. 2(a), both D and C_e converge with the reduction in Δx at the constant interface width parameter $\epsilon = 4.0$. The difference is attributed to the calculation of the induced charge density ρ_e, as demonstrated in Fig. 2(c) and (e), especially in the x direction. In addition, the electric field distribution at the droplet-matrix interface is also modified which can be noticed in the inset of Fig. 2(d). And only subtle variance is observed in the concentration distribution of Fig. 2(f). To achieve acceptable accuracy and save calculation time, we adhere to $\Delta x = 1.0$ in the following parts.

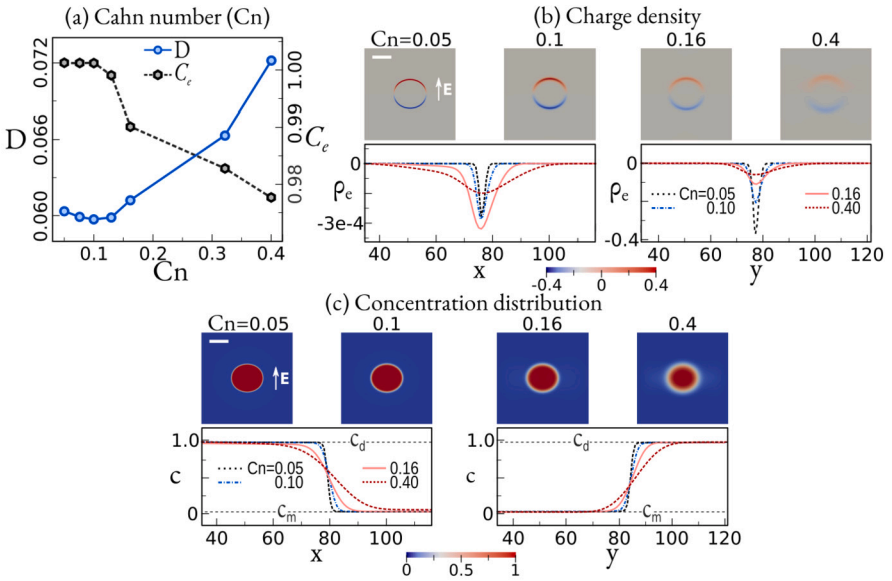

Fig. 3. (a) The verification with the Cahn number ($\mathrm{Cn} = w/d_0$). Blue dots: deformation factor D with Cn; black hexagons: surface charge density C_e with Cn. (b) Charge density at $t = 10^4$. Upper row: charge density distribution; lower row: intersections along x and y directions. The upper and lower domain borders are constrained with the electric potential $\Psi_t = 10$ and $\Psi_0 = 0$, respectively. The scale bar denotes 50 and the colorbar scales ρ_e. (c) Concentration field at $t = 1e4$ with the colorbar below measures the droplet concentration.

7.3. Interface width-Cahn number Cn

In the second part, the influence of the interface width w on the numerical accuracy is discussed. Here, we alter the model parameter ϵ in the free energy density functional Eq. (1) from 0.5 to 4.0. In this way, the so-called Cahn number $\mathrm{Cn} = w/d_0$ to express the ratio of the interface width to the droplet diameter. By setting a larger ϵ, the interface width increases, and so as Cn. The result in Fig. 3(a) implies that both the deformation factor D and the surface charge density C_e indicate $\mathrm{Cn} = 0.1$ ($\epsilon = 4.0$) to be a good compromise between accuracy and calculation speed.

Here, we address that the surface charge density C_e is the key value of the verification process, rather than the charge density ρ_e. With the widened interface with Cn, the composition gradient ∇c reduces (see Fig. 3(c)) which results in the decreasing permittivity gradient $\nabla\varepsilon = (\mathrm{d}\varepsilon/\mathrm{d}c)\nabla c$. While the surrounding electric potential Ψ is hardly modified, for there are not huge amounts of induced charges in our simulations. Resulting from this, the calculated ρ_e by the Poisson equation changes with Cn as

$$\nabla\cdot(\varepsilon\nabla\Psi) = \nabla\varepsilon\cdot\nabla\Psi + \varepsilon\nabla^2\Psi = \frac{\mathrm{d}\varepsilon}{\mathrm{d}c}\nabla c\cdot\mathbf{E} + \varepsilon\nabla^2\Psi = -\rho_e. \tag{32}$$

In fact, according to the Gaussian law, the induced charge wrapped by a closed surface should be irrelevant to the interface width. Hence, we choose the more appropriate C_e as the criterion for deciding the resolution Δx and interface width parameter ϵ, rather than the charge density ρ_e.

7.4. Residual threshold eps and time step Δt

In this part, we focus on the numerical accuracy of solving the Navier-Stokes equation and Poisson equation. Two factors are investigated, namely the residual threshold eps and the time step Δt. Here, eps controls the accuracy of the Poisson equation solutions for the Navier-Stokes equation, as well as the Gaussian equation. When the absolute residual values of these two equations become smaller than the preset eps, the iteration stops and returns the velocity $\mathbf{u}$ and electric potential Ψ. As illustrated in Fig. 4, the deformation factor D shows hardly any prominent influence by eps and Δt. But the surface charge density C_e converges as $\mathrm{eps} \le 1e-8$ and $\Delta t \le 1e-4$. So we choose $\mathrm{eps} = 1e-8$ in all other simulations of this work.

7.5. Energy stability of the numerical method

In this part, we confirm numerically the energy stability of the Cahn-Hilliard-Navier-Stokes-Gauss model Eq. (24). We use the same setup and modeling parameters as in Sec. 7.2, and choose three distinct values of the time step Δt. As demonstrated in Fig. 5, the total energy of the system has an apparent oscillation at $t < 5e2$ which is attributed to the intrinsic shortage of the explicit Euler method. Afterwards, the simulations with $\Delta t \le 1e-3$ show the continuous energy decrease with time until the final equilibrium state is reached. However, by choosing inappropriately large time step, $\Delta t = 1e-2$, the total energy is erroneously increasing gradually with time. A further increase in the time step leads to numerical instability. The presented tests in Fig. 5, altogether with the restriction for the time step resulting from the von Neumann stability analysis in the supplementary Sec. I. E, prove the energy stability and

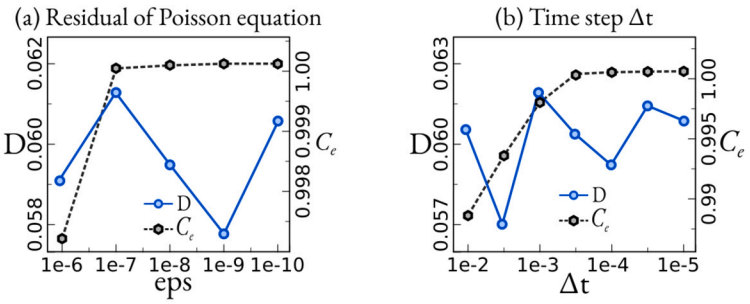

Fig. 4. (a) Convergence of the droplet deformation factor D and the surface charge density C_e with (a) the residual threshold of Poisson equation eps and (b) the time step Δt.

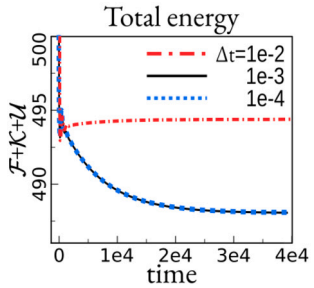

Fig. 5. Total energy dissipation of the droplet by electrostriction with the reduction in the time step Δt.

accuracy of our CHNSG model for relatively small time step. In the following sections, we choose a feasible, but small time step $\Delta t = 1e-4$ which is less than the one obtained by the stability analysis of Cahn-Hilliard-Navier-Stokes equations in Ref. [63]. A fully unconditional energy stability scheme needs to be heedfully discussed in future works.

8. Model verification with Taylor's theory

For the leaky dielectric droplet inside the electric field, its shape is deformed into an ellipse. The deformation factor D has been deduced as a function of permittivity ratio $\varepsilon_d/\varepsilon_m$, conductivity ratio σ_d/σ_m, and the electro-capillary number Ca_E. In Ref. [1], Taylor derived the deformation factor

$$D = \frac{9\,\mathrm{Ca}_E}{16}\frac{(\sigma_d/\sigma_m)^2 + 1.5\,\sigma_d/\sigma_m - 3.5\,\varepsilon_d/\varepsilon_m + 1}{(\sigma_d/\sigma_m + 2)^2}. \tag{33}$$

Another derivation in 2-dimensional case is achieved by Feng [3] who presents the following expression,

$$D = \frac{\mathrm{Ca}_E[(\sigma_d/\sigma_m)^2 + \sigma_d/\sigma_m - 3\,\varepsilon_d/\varepsilon_m + 1]}{3(\sigma_d/\sigma_m + 1)^2}. \tag{34}$$

In the following parts, we validate our model by changing the permittivity ratio $\varepsilon_d/\varepsilon_m$, conductivity ratio σ_d/σ_m between droplet and matrix, and the electro-capillary number Ca_E. The simulated droplet deformation factor D is compared with both Eqs. (33) and (34).

8.1. Permittivity ε

The initial setup is identical to Sec. 7.2, as shown in Fig. 2(b). The permittivity ratio $\varepsilon_d/\varepsilon_m$ varies from 0.1 to 100. The simulated deformation factor presents two behaviors, as depicted in Fig. 6(a). At $\varepsilon_d/\varepsilon_m < 10.3$, $D < 0$ denotes a prolate droplet shaped under the electric field. While for the setup with $\varepsilon_d/\varepsilon_m > 10.3$, the droplet is stretched in the horizontal direction forming an oblate ellipse with $D > 0$. The droplet morphology snapshots in Fig. 6(b) clearly demonstrate the shape changing from prolate to oblate with increasing $\varepsilon_d/\varepsilon_m$. Compared with Eqs. (33) and (34), a better match gives credit to Feng at a larger permittivity ratio, and the droplets with $\varepsilon_d/\varepsilon_m \leq 1.0$ are more consonant with Taylor's theory. As discussed in previous researches [20,26], the droplet deformation is propelled by the induced interfacial charges, which change signs at $\varepsilon_d/\varepsilon_m = 10.3$ (see Fig. 6(b)). Resulting from this, the Coulomb force and the dielectric force trigger the fluid flow tangent to the droplet interface. For $\varepsilon_d/\varepsilon_m > 10.3$, the material flows from pole to equator, while reversed at $\varepsilon_d/\varepsilon_m < 10.3$, which is illustrated by the velocity vectors in Fig. 6(d). Consequently, the droplet shows diverse ending equilibrium morphologies.

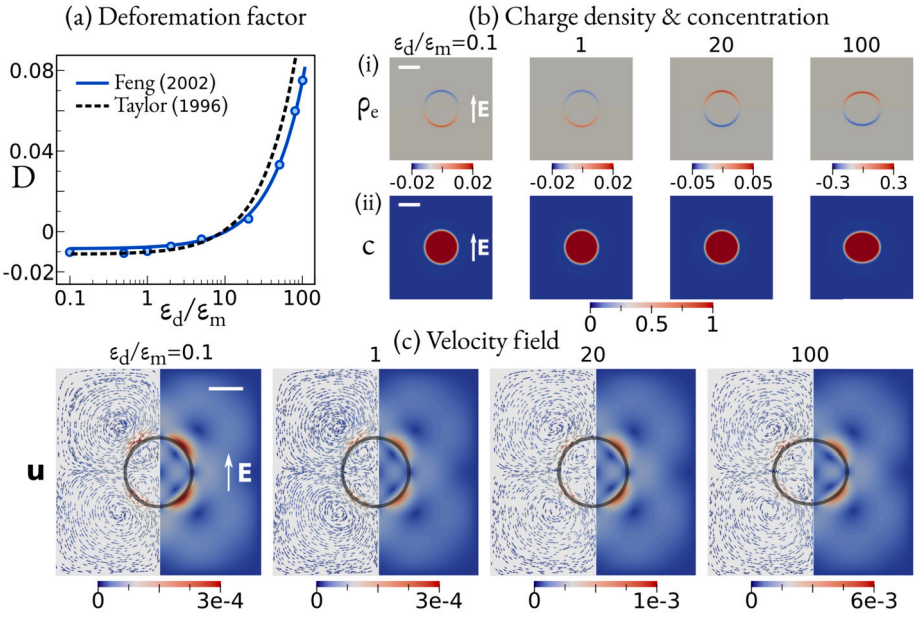

Fig. 6. (a) The droplet deformation factor D with the permittivity ratio $\varepsilon_d/\varepsilon_m$ between droplet and matrix, compared with Taylor's (black dashed line) and Feng's theory (blue solid line). (b)(i) The charge density ρ_e and (ii) the concentration distribution c. (c) Left half panel: the velocity field $\mathbf{u}$; right half panel: $|\mathbf{u}|$ scaled by the color bar below. The gray circles mark the droplet interfaces.

8.2. Conductivity σ

Next, the conductivity ratio between the droplet and matrix σ_d/σ_m is varied from 0.5 up to 100.0 at the constant permittivity ratio $\varepsilon_d/\varepsilon_m = 80.0$. All other simulation parameters are identical to Sec. 8.1. The comparison with Taylor and Feng's theory is demonstrated in Fig. 7 and the good consistency of the droplet deformation factor D with Feng's equation (blue solid line) can be observed.

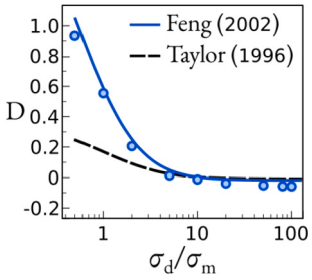

Fig. 7. The droplet deformation factor D with the conductivity ratio σ_d/σ_m between droplet and matrix, compared with Taylor's (black dashed line) and Feng's theory (blue solid line).

8.3. Electro-capillary number Ca_E

Next, we alter the electro-capillary number Ca_E. Here, two scenarios are considered, the oblate and prolate droplet (named after the final morphology). Setting the permittivity ratio $\varepsilon_d/\varepsilon_m = 80.0$ and the conductivity ratio $\sigma_d/\sigma_m = 5.0$, the droplet deformation factor D shows a linear relationship with Ca_E, as guided by the blue dashed line in Fig. 8(a)(i). Similarly, for the prolate drops, by choosing $\varepsilon_d/\varepsilon_m = 1.75$ and $\sigma_d/\sigma_m = 3.5$, $D \propto \mathrm{Ca}_E$ is in good agreement with Feng's theory. Some discrepancies are expected at large Ca_E setups where the droplet interface deviates from the elliptical shape. Clearly noticeable in Fig. 8(b), the interface position marked by the red dots for $\mathrm{Ca}_E = 10.0$ shows large mismatches with the solid ellipse line fitted with the least squares method. In this way, both Taylor and Feng's analytical equations are incapable of describing the real stretched interface. In our model, we observe another mechanism attributing to this derivation which is not considered in previous researches. As we compare the concentration distribution along the interface between different Ca_E in Fig. 8(c)(i), the interface widens itself and the matrix equilibrium concentration increases with Ca_E. It indicates that the thermodynamic equilibrium is modified by the external field.

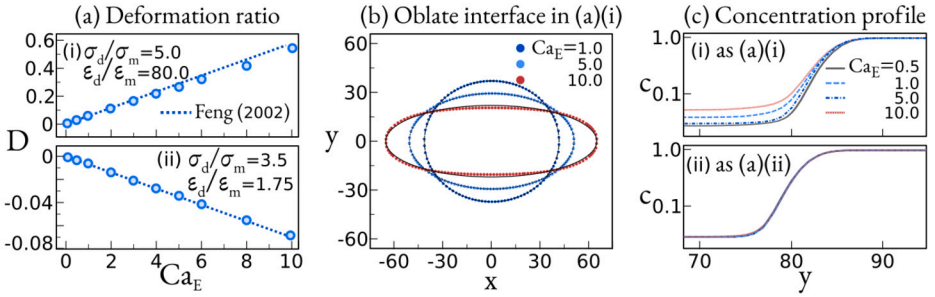

Fig. 8. (a) The droplet deformation factor D with the electro-capillary number Ca_E, compared with Feng's theory (blue dashed lines), (i) oblate droplets; (ii) prolate drops. (b) The droplet interface with various Ca_E of the oblate drops. Dots: simulated interface positions with $c = 0.5$; lines: elliptical fitting with the least squares method. (c) concentration profiles of the interface intersected at x = 0, (i) oblate; (ii) prolate.

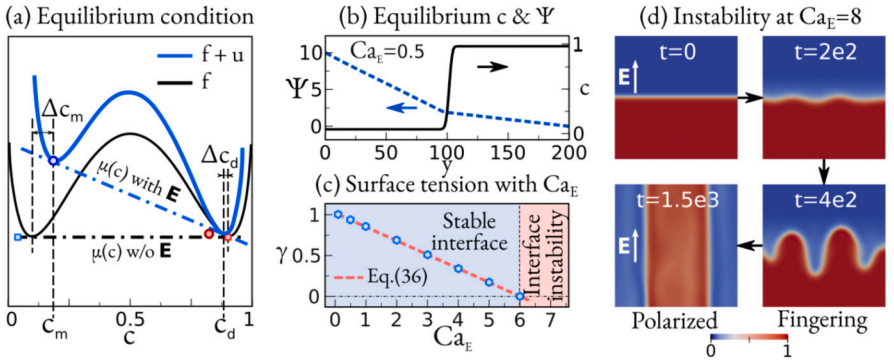

Fig. 9. (a) The schematic equilibrium condition. The free energy densities with and without the electric field strength **E** are depicted with the solid blue and black lines, respectively. The dot-dashed lines are the common tangent at equilibrium, with the open dots marking the equilibrium compositions c with **E** and open squares for c without **E**. (b) The equilibrium concentration c and electric potential Ψ at $t = 1e5$ with the electro-capillary number $\mathrm{Ca}_E = 0.5$. (c) Droplet-matrix interfacial tension $\gamma < 0$ with Ca_E number. The simulated values (open dots) fall on the theoretical line with Eq. (36). The red-colored region highlights the interfacial instability with $\gamma < 0$ at $\mathrm{Ca}_E \geq 6.0$. (d) The interface instability evolves with time at $\mathrm{Ca}_E = 8.0$. The color bar scales the composition.

9. Thermodynamics with electric fields

To study the electro-thermodynamic equilibrium, a flat droplet-matrix interface is considered, as illustrated in Fig. 9(d)($t = 0$), where the curvature effect is negligible inside the bulk regions with $\kappa\epsilon\nabla^2 c = 0$. In this way, the simplified electrochemical potential reads

$$\mu(c) = \frac{\partial f}{\partial c} - \frac{\partial u}{\partial c} = \frac{\partial f}{\partial c} - \frac{\mathrm{Ca}_E}{2}(\varepsilon_d - \varepsilon_m)\mathbf{E}^2. \tag{35}$$

Due to the difference of the conductivity $\sigma(c) = \sigma_d c + \sigma_m(1-c)$, the electric field strength $\mathbf{E}_m$ inside the bulk matrix becomes larger than $\mathbf{E}_d$ amid the bulk droplet, as shown by the simulated equilibrium electric field in Fig. 9(b). Moreover, the electric field strength **E** changes the energy state of the droplet and matrix, leading to the right-lopsided free energy density $f + u$ which is schematically illustrated in Fig. 9(a). At equilibrium, the new equilibrium compositions c_m and c_d of each phase are established by the tilted blue dot-dashed common tangent line. In the matrix phase, the equilibrium concentration c_m shows a larger deviation Δc_m than Δc_d inside the droplet. Due to the equilibrium concentration changes, the surface tension is affected by the electric field and can be expressed by the following integral from $y = 0$ to ∞ as

$$\begin{aligned}\gamma &= \int_0^\infty \left[\Delta f(y) + \Delta u(y) + \frac{\kappa\epsilon}{2}(\nabla c)^2\Big|_y - \frac{\mathrm{Ca}_E}{2}\varepsilon\left(\nabla\Psi\right)^2\Big|_y\right]\mathrm{d}y \\ &= \int_0^\infty \left[\kappa\epsilon(\nabla c)^2 - \mathrm{Ca}_E\varepsilon\mathbf{E}^2\right]\mathrm{d}y \\ &= \gamma^* - \mathrm{Ca}_E\int_0^\infty \varepsilon\mathbf{E}^2\mathrm{d}y.\end{aligned} \tag{36}$$

Testified in our simulations shown in Fig. 9(c), the surface tension γ follows the linear relationship with Ca_E. A further increase in the electric effect can result in interface instability. As demonstrated in Fig. 9(d) with $\mathrm{Ca}_E = 8.0$, the interface starts to oscillate and

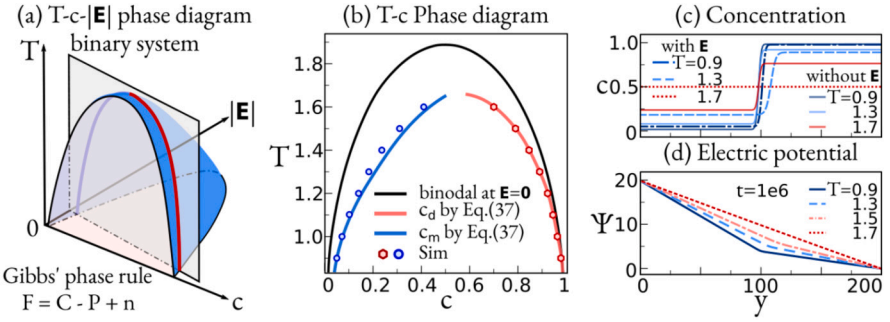

Fig. 10. (a) The schematic phase diagram (PD) of the binary fluid system with temperature T-composition c-electric field strength $|\mathbf{E}|$ obeying the Gibbs' phase rule. (b) The binodal compositions with temperature T are influenced by the electric field and deviate from the black binodal line ($\mathbf{E}=0$). Open dots: simulation as in (c) and (d); solid colored lines: theory with Eq. (37). (c) Equilibrium concentration profile across the interface with temperature T at $\mathbf{E}=\mathbf{0}$ (solid lines) and with $\mathbf{E}$ (dashed lines) as (ii). (d) Equilibrium electric potential Ψ with temperature T at $t=1e6$ with $\Psi_1=20$ at $y=0$ and $\Psi_0=0$ at $y=200$. Rest parameters are identical to Fig. 2.

develops the fingering morphology at $t=4e2$. Finally, the droplet phase gets polarized and its interface lays parallel to the electric field direction at $t=1.5e3$. With further enhancing the dielectric force, the surface tension converges to zero.

Inferring from the above discussion, we emphasize two crucial mechanisms contributing to the fluid deformation inside the electric field. (i) The dielectric force proportional to $-\sum_{i=1}^{N} c_i(\delta u/\delta c_i) - \rho_e(\delta u/\delta \rho_e)$ (see Eq. (23)). (ii) The droplet surface tension reduction proportional to $-\mathrm{Ca}_E \varepsilon \mathbf{E}^2$. Resulting from this, the fluid gets stretched and expands its surface area most rapidly in the direction with the largest surface tension decrease. The electric field induced surface tension drop is vastly ignored in previous researches and should be carefully scrutinized for the surface tension force treatment in the front-tracking simulation methods, such as LS and VOF.

In addition, we suggest a more complex phase diagram for the binary fluids inside the electric field, as illustrated in Fig. 10(a). According to Gibbs' phase rule, the degree of freedom $\mathrm{F}=\mathrm{C}-\mathrm{P}+\mathrm{n}$ is decided by the component number $\mathrm{C}=2$, the phase number P, and the external factor number n. In isobaric cases, $\mathrm{n}=2$ represents the two decisive factors, namely the temperature T and electric field strength $\mathbf{E}$. Theoretically, the equilibrium compositions c_m and c_d can be calculated with

$$\begin{aligned} \mu(c_m) &= \mu(c_d) = \mu_e, \\ \left[f(c_m)+u(c_m)\right] - \left[f(c_d)+u(c_d)\right] &= \mu_e(c_m - c_d), \\ |\mathbf{E}_m| = \frac{\Psi_1-\Psi_0}{L}\frac{\sigma(c_d)}{\sigma(c_m)+\sigma(c_d)}, \quad |\mathbf{E}_d| &= \frac{\Psi_1-\Psi_0}{L}\frac{\sigma(c_m)}{\sigma(c_m)+\sigma(c_d)}. \end{aligned} \tag{37}$$

Instead of the binodal line, the equilibrium composition is expressed by a 3-dimensional binodal surface, as highlighted in Fig. 10(a). Simulated at various temperatures T; see Fig. 10(c) and (d), the T-c phase diagram for the binary fluid system at $\mathrm{Ca}_E = 1.0$ is recovered in Fig. 10(b). Both c_m (blue open dots) and c_d (red open dots) deviate largely from the black solid $\mathbf{E}$-free binodal line and show good consistencies with the theoretical colored binodal lines calculated via Eq. (37).

10. Dynamics with capillary wave theory

In the previous section, thermodynamics, especially the equilibrium states, are discussed. In this section, we study energy dissipation with the help of the capillary wave theory (CWT). For liquid surfaces perturbed by small thermal noises, its energy dissipation obeying CWT has been proved by several experiments [64,65]. When the perturbation is small, the increase in the surface energy ΔE is proportional to the change in the surface area as

$$\Delta E \approx \frac{\gamma}{2}\int \left(\nabla h\right)^2 \mathrm{d}x\,\mathrm{d}y, \tag{38}$$

where the interface position h is marked by the location with the droplet composition $c=0.5$. After Fourier transformation, Eq. (38) is rewritten as

$$\Delta E(q) = \frac{\gamma}{2}\int q^2 \left|\Delta\widetilde{h}(q)\right|^2 \mathrm{d}q,$$

where q denotes the wave frequency, and $\Delta\widetilde{h}^2(q)$ stands for the capillary wave amplitude. At equilibrium, each wave mode of the fluctuation has the energy of $k_B T$, which says

$$\left\langle \Delta\widetilde{h}^2(q)\right\rangle = \frac{k_B T}{4\pi^2 q^2 \gamma}. \tag{39}$$

To validate the energy dissipation of the droplet interface in our electro-hydro-thermodynamic model, a flat fluid-fluid interface is placed in the center of a 100×100 domain, as shown in Fig. 11(a)(i). The rest setups are identical to Sec. 8.3. Perturbed by the

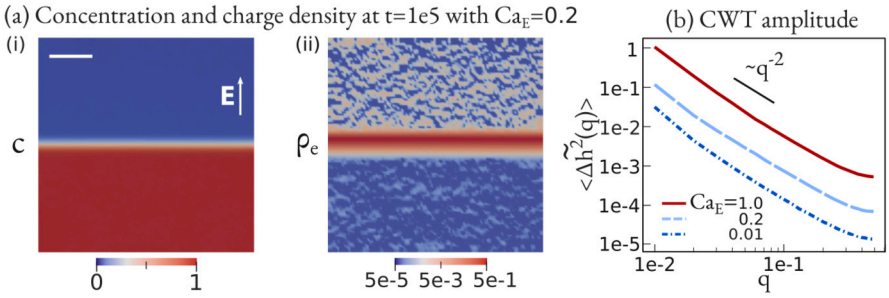

Fig. 11. (a) The exemplary composition c and charge density ρ_e perturbed by the composition noise $\xi_c = (0.01, 0.01)$ at $t = 1e5$ with $\mathrm{Ca}_E = 0.1$. The color bar of ρ_e value is in log-scale. (b) The capillary wave amplitudes $\langle \Delta\widetilde{h}^2(q) \rangle$ with the wave frequency q for different Ca_E numbers. The black solid line guides $\langle \Delta\widetilde{h}^2(q) \rangle \sim q^{-2}$.

Table 1
Simulation parameters for the ternary system.

Parameters	Description	Values
$\chi_{12}, \chi_{13}, \chi_{23}$	Flory parameters	2.5, 2.5, 2.5
χ_{123}	Triple interaction parameter	3.5
κ	Surface tension parameter	1.0
ϵ	Interface width parameter	4.0
D_1, D_2, D_3	Diffusivity for each component	1.0, 1.0, 1.0
ρ_1, ρ_2, ρ_3	Density for each component	1.0, 1.0, 1.0
η_1, η_2, η_3	Viscosity for each component	1.0, 1.0, 1.0

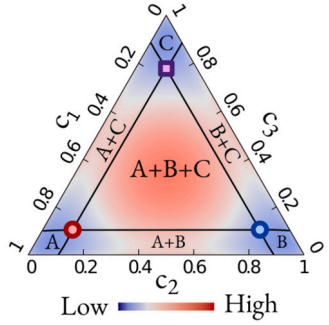

Fig. 12. Ternary phase diagram of an A-B-C system, on which the equilibrium compositions of A, B, and C are marked by the red open dot, blue open dot, and purple open square, respectively. The parameters of free energy density are tabulated in Table 1. The color bar measures the free energy density magnitude.

compositional fluctuation with the amplitude of $\xi_c = (0.01, 0.01)$, the induced charges are clearly visible at both interface and the bulk regions, as demonstrated in Fig. 11(a)(ii). This observation is totally distinct from the charge distribution without noise; see Fig. 2(b). By varying Ca_E from 0.01 to 1.0, the capillary wave amplitude $\left\langle \Delta\widetilde{h}^2(q) \right\rangle$ in Fig. 11(b) not only shows the q^{-2} scaling law predicted by the CWT, but also magnifies with the increase in Ca_E. This observation indicates that the leaky dielectric droplet still follows CWT, which suggests the energy dissipation via surface energy reduction.

11. Result and discussion

In this section, we discuss the droplet coalescence and spinodal decomposition of an A-B-C ternary system with the electro-hydro-thermodynamic model. Choosing the free energy parameters in Table 1, the ternary phase diagram in Fig. 12 has three local minimal states, as marked by the red open dot for component 1 rich phase A, the blue open dot for component 2 dense phase B, and the purple open square for C. The corresponding equilibrium compositions for phases A, B, and C are $(0.770, 0.115, 0.115)$, $(0.115, 0.770, 0.115)$, and $(0.115, 0.115, 0.770)$, respectively.

11.1. Ternary droplet coalescence

For binary system, abundant previous results [20] are available for the droplet coalescence with electro-hydrodynamics. The droplets merge by minimizing the surface energy, resulting in the final morphology of a single droplet. With our multi-component model, we elucidate the ternary droplet coalescence by placing the red droplet (component 1 riched phase A) and another blue droplet (component 2 dense phase B) in a 240×480 purple matrix (phase C) domain. The initial droplet radii are 40 and their spacing is set to be 40, as shown in Fig. 13(a)(i). The external electric field parallel to the x-direction is applied with $\Psi_1 = 24.0$ at the

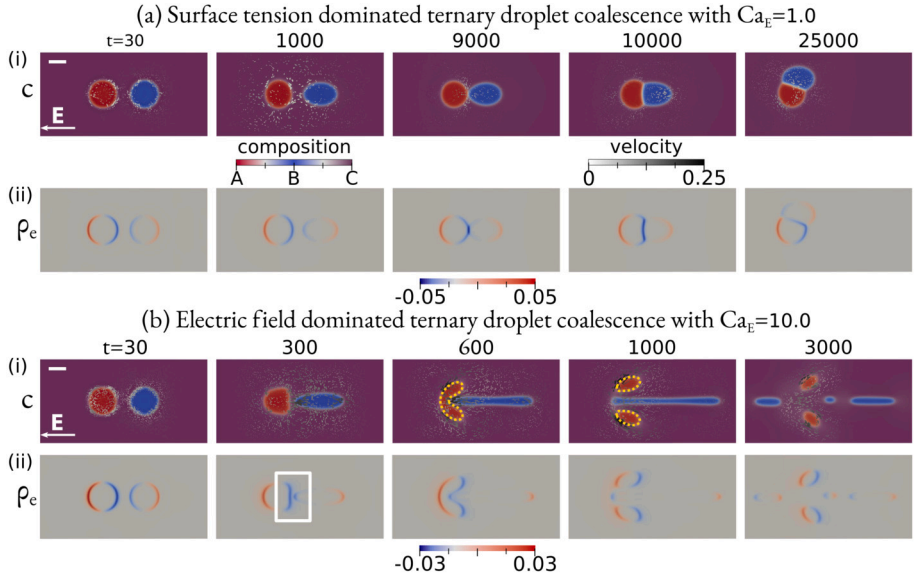

Fig. 13. Ternary droplet coalescence coupled with electro-hydrodynamics. (a) Surface tension dominant coalescence with a weak electrostatic effect, $\mathrm{Ca}_E = 1.0$. (i) The composition field c evolves with time and the color bar shows red for droplet A, blue for droplet B, and purple for matrix C. The velocity field is stacked on the same figure. (ii) The evolution of the charge density ρ_e with time and the values are scaled by the color bars beneath the figure. (b) The electric field dominated droplet motion with a strong electrostatic effect, $\mathrm{Ca}_E = 10.0$. The velocity magnitude is measured by the vector cone size, as well as the white-black color bar.

left boundary and $\Psi_0 = 0$ at the right. Here, the conductivity for each component is assigned to be $(\sigma_1, \sigma_2, \sigma_3) = (5.0, 1.0, 1.0)$ and a special permittivity setup is chosen as $(\epsilon_1, \epsilon_2, \epsilon_3) = (50.0, 1.0, 5.0)$.

Clearly noticeable in charge density distribution in Fig. 13(a)(ii), the selected permittivity ratio emerges the negative charges at the right side of droplet A, directly towards the charges with the same sign on the left side of droplet B. This scenario can never take place in the binary system and the repulsive Coulomb force of the same charges can magnificently alter the droplet coalescence. By setting a weak electric capillary effect with $\mathrm{Ca}_E = 1.0$, the surface tension overwhelms the electric forces. The Coulomb force scaled by Ca_E is too weak to stop the aggregation of the negative charges. At $t = 1e4$, the droplets merge into a Janus particle which is composed of the oblate droplet A and prolate drop B, as depicted in Fig. 13(a). After coalescence, the Janus droplet experiences the so-called Quincke rotation [66,67] counterclockwise. Similar morphological transformations are reported in the Janus droplet [68] and double-emulsion droplet [69].

With further increasing Ca_E to 10.0, the droplet coalescence is entirely denied by the repulsive Coulomb force between A and B, as highlighted by the white squares in Fig. 13(b)(ii). The left interface of the red droplet A is firstly deformed into a concave shape, and finally cut into 2 small droplets, as marked by yellow dashed lines in Fig. 13(b)(i). Moreover, the strong electrostatic force propels the fluid flow in the whole domain, causing the instability of the elongating blue droplet B which ruptures into 3 satellite drops at $t = 3e3$. Similar droplet breakup has been observed in the electrospinning process [70] and needs to be heeded in future works.

11.2. Ternary spinodal decomposition

In this part, the influence of electrohydrodynamics on the ternary spinodal decomposition is elucidated. Initially, a homogeneous 200×200 domain with composition $\boldsymbol{c} = (0.33, 0.33, 0.34)$ is perturbed by the composition noise with amplitude of $\boldsymbol{\xi}_c = (0.01, 0.01, 0.01)$. The permittivity and conductivity are set to be $(50.0, 25.0, 1.0)$ and $(5.0, 3.0, 1.0)$, and the electric field setup is identical to sec. 7.2. Triggered by noises, the phase separation starts and produces a huge amount of interfaces, as shown in Fig. 14(a)(i). Due to the selected permittivity ratio, the purple phase C is stretched in y direction by the electric force, while the red phase A elongates in the x direction which is highlighted by the yellow dot-dashed line in Fig. 14(a)(i). Since the weak electro-capillary effect with $\mathrm{Ca}_E = 1.0$ is adopted, the surface tension dominates the morphological evolution. The inhomogeneous surface tension induced the so-called Marangoni flow which propels the droplet coalescence. In the white squares of Fig. 14(a)(i), the Marangoni flow is sketched by the gray cones. Large flow velocity appears when droplets merge and the fluid flow behaves vastly like the laminar flow with direction perpendicular to the interfaces. Consequently, the final morphology shows only a subtle difference from the spinodal structures with slightly deformed droplets.

By increasing Ca_E to 10.0, the electric effect becomes dominant. The fluid flow is no longer decided by the surface tension itself, and its direction is highly correlated with the charge distribution. Highlighted in the white dashed squares in Fig. 14(b), negative charges are induced at the left interface of the purple droplet C, and positive charges on the right side. Therefore, the Coulomb's force results in the upwards fluid flow tangent to the left interface, while the downstream appears on the right. Consequently, the vortex marked by the white "⊗" symbol is produced which rotates the droplet C clockwise. Moreover, the vortex expands to the entire domain until damped by the viscous effect, and results in the rotation of the whole domain. Consequently, the phase separation

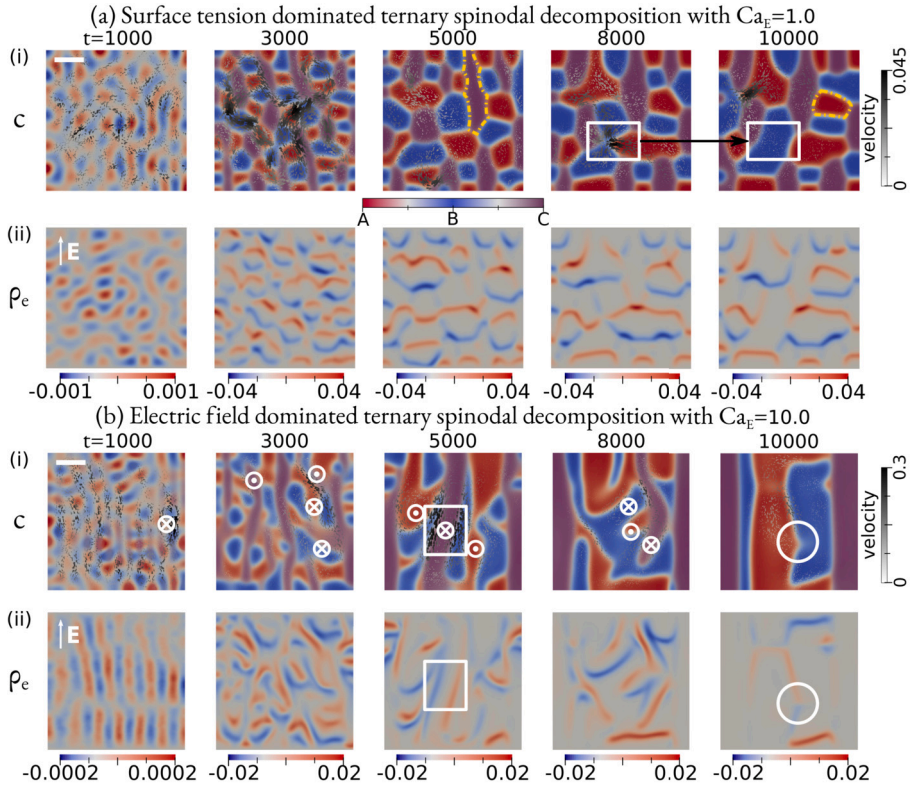

Fig. 14. Ternary spinodal decomposition (SP) coupled with electro-hydrodynamics. (a) Surface tension dominant SP with weak $Ca_E = 1.0$. (i) The composition c stacked by the velocity field (gray cones). Two stretched droplets are highlighted with yellow dot-dashed lines. (ii) The charge density ρ_e evolution scaled by the color bars below. (b) The electric field dominated SP with strong $Ca_E = 10.0$. Some charge-induced vortices are highlighted in white "⊗/⊙" symbols obeying the right-hand rule.

morphology deviates largely from the spinodal structure in Fig. 14(a). In addition, we find the transient state in the white circles in Fig. 14(b). Different from the surface tension dominated scenario, the zigzag interface is stabilized by the electric field. Finally, when the induced charges get gradually dissipated by the conduction, all droplets get polarized, forming a lamellar structure parallel to the external field.

12. Conclusion

In conclusion, we present a multi-component electro-hydro-thermodynamic model to investigate the droplet behaviors affected by the interplay of diffusion, hydrodynamics, and electric field. The total energy functional for both leaky and perfect dielectric materials is derived and the corresponding energy law is presented. The verification of our model with Taylor and Feng's classic theories is performed in 2D. Most importantly, differing from the previous models, the expression of the electrochemical potential μ is revisited and the dielectric-related correction term is added to recapitulate the models. The modification in the chemical potential leads to a generalized electro-hydro-thermodynamic force including the Kortweg stress and the Maxwell stress. Consequently, the thermodynamic equilibrium is deeply impacted by the electric field which explains the surface tension reduction induced by the electric field that has been observed in many experiments. In addition, our multi-component model enables us to study the ternary droplet coalescence and spinodal decomposition, bringing some interesting observations that can hardly be scrutinized in the binary system. We expect that the present model will help to understand the electrohydrodynamic behaviors of complex droplet systems and deepen our knowledge of droplet/fluid manipulation by the electric field, for instance, in the electrospinning process. Other suggestions for future work could be the electro-wetting/dewetting and ionized surfactant-related phenomena.

CRediT authorship contribution statement

Haodong Zhang: Writing – review & editing, Writing – original draft, Visualization, Validation, Software, Methodology, Investigation, Formal analysis, Data curation, Conceptualization. **Fei Wang:** Writing – review & editing, Writing – original draft, Supervision, Software, Methodology, Investigation, Formal analysis, Conceptualization. **Britta Nestler:** Writing – review & editing, Supervision, Resources, Funding acquisition.

Declaration of competing interest

The authors declare that they have no known competing financial interests or personal relationships that could have appeared to influence the work reported in this paper.

Data availability

Data will be made available on request.

Declaration of generative AI and AI-assisted technologies in the writing process

During the preparation of this work, H. Zhang used ChatGPT 3.5 to check grammar and improve language. After using this tool/service, H. Zhang reviewed and edited the content as needed and takes full responsibility for the content of the publication.

Acknowledgements

H.D. Zhang thanks for funding of the research through the Gottfried-Wilhelm Leibniz prize NE 822/31-1 of the German Research Foundation (DFG). F. Wang is grateful to the VirtMat project P09 “Wetting Phenomena” of the Helmholtz Association (MSE-programme No. 43.31.01). The authors acknowledge support from the state of Baden-Württemberg through bwHPC.

Appendix A. List of symbols

Notation	Description
Ω	Domain investigated
S	Domain boundary
$\mathcal{L}$	Total energy functional
$\mathcal{F}$	Chemical free energy functional
$\mathcal{K}$	Kinetic energy
$\mathcal{U}$	Electric potential energy
g	Chemical free energy density
f	Bulk free energy density
c_i	Concentration of composition i
c_d	Equilibrium droplet concentration
c_m	Equilibrium matrix concentration
N	Number of components
μ	Electrochemical potential
χ	Flory interaction parameter
γ	Surface tension
κ	Surface tension parameter
ϵ	Interface width parameter
R_g	Gas constant
v_m	Molar volume
T	Temperature
t	Time
D_i	Diffusivity of component i
τ	Kinetic parameter for Allen-Cahn model
ξ_a	Thermal phase variable noise amplitude
δ_K	Kronecker’s delta
λ	Lagrange multiplier
p	Hydrostatic pressure
P	Grand potential
ρ	Density
η	Dynamic viscosity
$\langle \Delta\tilde{h}^2(q) \rangle$	Capillary wave amplitude
q	Capillary wave frequency
u	Electrical energy density
Ψ	Electric potential
σ	Conductivity
ε	Permittivity
ρ_e	Charge density
C_e	Surface charge density

D	Droplet deformation factor
Δx	Mesh resolution
Δt	Simulation time step
eps	Poisson equation residual threshold
Pé	Pélect number
Cn	Cahn number
We	Weber number
Re	Reynold number
Ca_E	Electro-capillary number
$\boldsymbol{c}$	Composition vector
$\boldsymbol{x}$	Position vector
$\mathbf{u}$	Macroscopic fluid velocity
ξ_c	Thermal composition noise amplitude
$\boldsymbol{f}_e$	Dielectric force
$\boldsymbol{f}_c$	Thermodynamic force
$\mathbf{E}$	Electric field strength
$\mathcal{M}$	Mobility
$\underline{\underline{\Theta}}$	Thermodynamic stress tensor
$\underline{\underline{\mathrm{T}}}$	Viscous stress tensor
$\underline{\underline{\sigma}}^M$	Maxwell stress tensor

Appendix B. Supplementary material

Supplementary material related to this article can be found online at https://doi.org/10.1016/j.jcp.2024.112907.

References

[1] G.I. Taylor, Studies in electrohydrodynamics. I. The circulation produced in a drop by an electric field, Proc. R. Soc. Lond. Ser. A, Math. Phys. Sci. 291 (1425) (1966) 159–166.
[2] J. Melcher, G. Taylor, Electrohydrodynamics: a review of the role of interfacial shear stresses, Annu. Rev. Fluid Mech. 1 (1) (1969) 111–146.
[3] J.Q. Feng, A 2D electrohydrodynamic model for electrorotation of fluid drops, J. Colloid Interface Sci. 246 (1) (2002) 112–121.
[4] J.A. Stratton, Electromagnetic Theory, vol. 33, John Wiley & Sons, 2007.
[5] D. Saville, Electrohydrodynamics: the Taylor-Melcher leaky dielectric model, Annu. Rev. Fluid Mech. 29 (1) (1997) 27–64.
[6] Y. Lin, Two-phase electro-hydrodynamic flow modeling by a conservative level set model, Electrophoresis 34 (5) (2013) 736–744.
[7] B. Van Poppel, O. Desjardins, J. Daily, A ghost fluid, level set methodology for simulating multiphase electrohydrodynamic flows with application to liquid fuel injection, J. Comput. Phys. 229 (20) (2010) 7977–7996.
[8] G. Tomar, D. Gerlach, G. Biswas, N. Alleborn, A. Sharma, F. Durst, S.W. Welch, A. Delgado, Two-phase electrohydrodynamic simulations using a volume-of-fluid approach, J. Comput. Phys. 227 (2) (2007) 1267–1285.
[9] Y. Zu, Y. Yan, A numerical investigation of electrohydrodynamic (ehd) effects on bubble deformation under pseudo-nucleate boiling conditions, Int. J. Heat Fluid Flow 30 (4) (2009) 761–767.
[10] P. Azizian, M. Azarmanesh, M. Dejam, M. Mohammadi, M. Shamsi, A. Sanati-Nezhad, A.A. Mohamad, Electrohydrodynamic formation of single and double emulsions for low interfacial tension multiphase systems within microfluidics, Chem. Eng. Sci. 195 (2019) 201–207.
[11] J. Sherwood, Breakup of fluid droplets in electric and magnetic fields, J. Fluid Mech. 188 (1988) 133–146.
[12] N. Gawande, Y. Mayya, R. Thaokar, Jet and progeny formation in the Rayleigh breakup of a charged viscous drop, J. Fluid Mech. 884 (2020) A31.
[13] A. Fernández, Response of an emulsion of leaky dielectric drops immersed in a simple shear flow: drops more conductive than the suspending fluid, Phys. Fluids 20 (4) (2008) 043303.
[14] S. Van der Pijl, A. Segal, C. Vuik, P. Wesseling, A mass-conserving level-set method for modelling of multi-phase flows, Int. J. Numer. Methods Fluids 47 (4) (2005) 339–361.
[15] A.Q. Raeini, M.J. Blunt, B. Bijeljic, Modelling two-phase flow in porous media at the pore scale using the volume-of-fluid method, J. Comput. Phys. 231 (17) (2012) 5653–5668.
[16] F. Wang, A. Choudhury, C. Strassacker, B. Nestler, Spinodal decomposition and droplets entrapment in monotectic solidification, J. Chem. Phys. 137 (3) (2012).
[17] Z. Qiao, S. Sun, Two-phase fluid simulation using a diffuse interface model with Peng–Robinson equation of state, SIAM J. Sci. Comput. 36 (4) (2014) B708–B728.
[18] X. Feng, Z. Qiao, S. Sun, X. Wang, An energy-stable smoothed particle hydrodynamics discretization of the Navier-Stokes-Cahn-Hilliard model for incompressible two-phase flows, J. Comput. Phys. 479 (2023) 111997.
[19] Z. Qiao, X. Yang, Y. Zhang, Thermodynamic-consistent multiple-relaxation-time lattice Boltzmann equation model for two-phase hydrocarbon fluids with Peng-Robinson equation of state, Int. J. Heat Mass Transf. 141 (2019) 1216–1226.
[20] Y. Lin, P. Skjetne, A. Carlson, A phase field model for multiphase electro-hydrodynamic flow, Int. J. Multiph. Flow 45 (2012) 1–11.
[21] D. Wang, Z. Abbas, Z. Du, Z. Du, L. Lu, K. Zhao, X. Zhao, Y. Yuan, H. Zong, Y. Cui, et al., Phase field simulation of electrohydrodynamic jet droplets and printing microstructures on insulating substrates, Microelectron. Eng. 261 (2022) 111817.
[22] Q. Yang, B.Q. Li, Y. Ding, 3d phase field modeling of electrohydrodynamic multiphase flows, Int. J. Multiph. Flow 57 (2013) 1–9.
[23] H. Tian, J. Shao, Y. Ding, X. Li, H. Liu, Numerical characterization of electrohydrodynamic micro-or nanopatterning processes based on a phase-field formulation of liquid dielectrophoresis, Langmuir 29 (15) (2013) 4703–4714.
[24] D. Jacqmin, Contact-line dynamics of a diffuse fluid interface, J. Fluid Mech. 402 (2000) 57–88.
[25] F. Wang, H. Zhang, Y. Wu, B. Nestler, A thermodynamically consistent diffuse interface model for the wetting phenomenon of miscible and immiscible ternary fluids, J. Fluid Mech. 970 (2023) A17.
[26] X. Liu, Z. Chai, B. Shi, A phase-field-based lattice Boltzmann modeling of two-phase electro-hydrodynamic flows, Phys. Fluids 31 (9) (2019) 092103.
[27] F. Wang, P. Altschuh, L. Ratke, H. Zhang, M. Selzer, B. Nestler, Progress report on phase separation in polymer solutions, Adv. Mater. 31 (26) (2019) 1806733.

[28] F. Wang, L. Ratke, H. Zhang, P. Altschuh, B. Nestler, A phase-field study on polymerization-induced phase separation occasioned by diffusion and capillary flow—a mechanism for the formation of porous microstructures in membranes, J. Sol-Gel Sci. Technol. 94 (2020) 356–374.
[29] J. Hua, L.K. Lim, C.-H. Wang, Numerical simulation of deformation/motion of a drop suspended in viscous liquids under influence of steady electric fields, Phys. Fluids 20 (11) (2008).
[30] F. Jiang, H. Liu, X. Chen, T. Tsuji, A coupled lbm-dem method for simulating the multiphase fluid-solid interaction problem, J. Comput. Phys. 454 (2022) 110963.
[31] Z. Chai, B. Shi, Simulation of electro-osmotic flow in microchannel with lattice Boltzmann method, Phys. Lett. A 364 (3–4) (2007) 183–188.
[32] L. Xu, L. Wang, N. Faraz, A thermo-electro-hydrodynamic model for vibration-electrospinning process, Therm. Sci. 15 (suppl. 1) (2011) 131–135.
[33] I. Roghair, H. van den Ende, F. Mugele, An openfoam-based electro-hydrodynamic model, in: 8th International Conference on Multiphase Flow, Jeju, Korea, 2013.
[34] H. Zhang, Y. Wu, F. Wang, F. Guo, B. Nestler, Phase-field modeling of multiple emulsions via spinodal decomposition, Langmuir 37 (17) (2021) 5275–5281.
[35] F. Wang, A. Choudhury, M. Selzer, R. Mukherjee, B. Nestler, Effect of solutal Marangoni convection on motion, coarsening, and coalescence of droplets in a monotectic system, Phys. Rev. E 86 (6) (2012) 066318.
[36] H. Zhang, F. Wang, B. Nestler, Line tension of sessile droplets: thermodynamic considerations, Phys. Rev. E 108 (5) (2023) 054121.
[37] F. Wang, P. Altschuh, A.M. Matz, J. Heimann, B.S. Matz, B. Nestler, N. Jost, Phase-field study on the growth of magnesium silicide occasioned by reactive diffusion on the surface of si-foams, Acta Mater. 170 (2019) 138–154.
[38] J. Kim, Phase field computations for ternary fluid flows, Comput. Methods Appl. Mech. Eng. 196 (45–48) (2007) 4779–4788.
[39] P. Yue, C. Zhou, J.J. Feng, Sharp-interface limit of the Cahn–Hilliard model for moving contact lines, J. Fluid Mech. 645 (2010) 279–294.
[40] R. Shimizu, H. Tanaka, A novel coarsening mechanism of droplets in immiscible fluid mixtures, Nat. Commun. 6 (1) (2015) 7407.
[41] Z. Guo, P. Lin, A thermodynamically consistent phase-field model for two-phase flows with thermocapillary effects, J. Fluid Mech. 766 (2015) 226–271.
[42] H. Zhang, F. Wang, B. Nestler, Janus droplet formation via thermally induced phase separation: a numerical model with diffusion and convection, Langmuir 38 (22) (2022) 6882–6895.
[43] Y. Wu, M. Kuzina, F. Wang, M. Reischl, M. Selzer, B. Nestler, P.A. Levkin, Equilibrium droplet shapes on chemically patterned surfaces: theoretical calculation, phase-field simulation, and experiments, J. Colloid Interface Sci. 606 (2022) 1077–1086.
[44] F. Wang, B. Nestler, A phase-field study on the formation of the intermetallic Al2Au phase in the Al–Au system, Acta Mater. 95 (2015) 65–73.
[45] V.P. Laxmipathy, F. Wang, M. Selzer, B. Nestler, Phase-field simulations of grain boundary grooving under diffusive-convective conditions, Acta Mater. 204 (2021) 116497.
[46] V.P. Laxmipathy, F. Wang, M. Selzer, B. Nestler, A two-dimensional phase-field study on dendritic growth competition under convective conditions, Comput. Mater. Sci. 186 (2021) 109964.
[47] P.C. Hohenberg, B.I. Halperin, Theory of dynamic critical phenomena, Rev. Mod. Phys. 49 (3) (1977) 435.
[48] A. Karma, W.-J. Rappel, Phase-field model of dendritic sidebranching with thermal noise, Phys. Rev. E 60 (4) (1999) 3614.
[49] H. Zhang, F. Wang, L. Ratke, B. Nestler, Brownian motion of droplets induced by thermal noise, Phys. Rev. E 109 (2024) 024208.
[50] J. Guo, C. Wang, S.M. Wise, X. Yue, An $h2$ convergence of a second-order convex-splitting, finite difference scheme for the three-dimensional Cahn–Hilliard equation, Commun. Math. Sci. 14 (2) (2016) 489–515.
[51] K. Cheng, W. Feng, C. Wang, S.M. Wise, An energy stable fourth order finite difference scheme for the Cahn–Hilliard equation, J. Comput. Appl. Math. 362 (2019) 574–595.
[52] C. Chen, X. Yang, Efficient numerical scheme for a dendritic solidification phase field model with melt convection, J. Comput. Phys. 388 (2019) 41–62.
[53] J. Yang, J. Kim, Numerical study of the ternary Cahn–Hilliard fluids by using an efficient modified scalar auxiliary variable approach, Commun. Nonlinear Sci. Numer. Simul. 102 (2021) 105923.
[54] Z. Liu, X. Li, The fast scalar auxiliary variable approach with unconditional energy stability for nonlocal Cahn–Hilliard equation, Numer. Methods Partial Differ. Equ. 37 (1) (2021) 244–261.
[55] D. Kay, R. Welford, Efficient numerical solution of Cahn–Hilliard–Navier–Stokes fluids in 2D, SIAM J. Sci. Comput. 29 (6) (2007) 2241–2257.
[56] J. Zhao, D. Han, Second-order decoupled energy-stable schemes for Cahn-Hilliard-Navier-Stokes equations, J. Comput. Phys. 443 (2021) 110536.
[57] X. Li, J. Shen, On fully decoupled msav schemes for the Cahn–Hilliard–Navier–Stokes model of two-phase incompressible flows, Math. Models Methods Appl. Sci. 32 (03) (2022) 457–495.
[58] C. Liu, R. Masri, B. Riviere, Convergence of a decoupled splitting scheme for the Cahn–Hilliard–Navier–Stokes system, SIAM J. Numer. Anal. 61 (6) (2023) 2651–2694.
[59] Z. Guo, P. Lin, J.S. Lowengrub, A numerical method for the quasi-incompressible Cahn–Hilliard–Navier–Stokes equations for variable density flows with a discrete energy law, J. Comput. Phys. 276 (2014) 486–507.
[60] F. Guillén-González, G. Tierra, Splitting schemes for a Navier-Stokes-Cahn-Hilliard model for two fluids with different densities, J. Comput. Math. (2014) 643–664.
[61] Y. Gao, D. Han, X. He, U. Rüde, Unconditionally stable numerical methods for Cahn-Hilliard-Navier-Stokes-Darcy system with different densities and viscosities, J. Comput. Phys. 454 (2022) 110968.
[62] A.J. Chorin, A numerical method for solving incompressible viscous flow problems, J. Comput. Phys. 135 (2) (1997) 118–125.
[63] V. Balashov, A. Zlotnik, On a new spatial discretization for a regularized 3D compressible isothermal Navier–Stokes–Cahn–Hilliard system of equations with boundary conditions, J. Sci. Comput. 86 (2021) 1–29.
[64] M.P. Fisher, D.S. Fisher, J.D. Weeks, Agreement of capillary-wave theory with exact results for the interface profile of the two-dimensional Ising model, Phys. Rev. Lett. 48 (5) (1982) 368.
[65] H.T. Davis, Capillary waves and the mean field theory of interfaces, J. Chem. Phys. 67 (8) (1977) 3636–3641.
[66] D. Das, D. Saintillan, Electrohydrodynamics of viscous drops in strong electric fields: numerical simulations, J. Fluid Mech. 829 (2017) 127–152.
[67] D. Das, D. Saintillan, A three-dimensional small-deformation theory for electrohydrodynamics of dielectric drops, J. Fluid Mech. 914 (2021) A22.
[68] X. Ji, R. Li, G. Liu, W. Jia, M. Sun, Y. Liu, Y. Luo, Z. Cheng, Phase separation-based electrospun Janus nanofibers loaded with rana chensinensis skin peptides/silver nanoparticles for wound healing, Mater. Des. 207 (2021) 109864.
[69] M.S. Abbasi, R. Song, J. Lee, Breakups of an encapsulated surfactant-laden aqueous droplet under a dc electric field, Soft Matter 15 (43) (2019) 8905–8911.
[70] A. Kaltbeitzel, K. Friedemann, A. Turshatov, C. Schönecker, I. Lieberwirth, K. Landfester, D. Crespy, Sted analysis of droplet deformation during emulsion electrospinning, Macromol. Chem. Phys. 218 (9) (2017) 1600547.